Precision Clinical Medicine, 2026, **9**: pbag003
https://doi.org/10.1093/pcmedi/pbag003
Published: 6 February 2026
Research Article

OXFORD

Therapeutic strategy for cervical gastric-type adenocarcinoma by targeting CLU to relieve CLU-associated stress and sensitize chemotherapy

Tong Wu[1,2,3,†], Xinyu Qu[1,2,3,†], Lili Jiang[1,2,3,†], Tingting Ren[1,2,3,†], Qinqin Liu[1,2,3], Xingyu Chang[1,2,3], Meng Xie[1,2,3,*], Keqin Hua[1,2,3,*], Junjun Qiu[1,2,3,*]

[1]Department of Gynecology, Obstetrics & Gynecology Hospital of Fudan University, Shanghai 200433, China
[2]Shanghai Key Lab of Reproduction and Development, Shanghai 200433, China
[3]Shanghai Key Lab of Female Reproductive Endocrine Related Diseaseses, Shanghai 200433, China
*Corresponding authors: Junjun Qiu, qiu_junjun@fudan.edu.cn; Keqin Hua, huakeqin@fudan.edu.cn; Meng Xie, ultrasonic2007@163.com
[†]Tong Wu, Xinyu Qu, Lili Jiang, and Tingting Ren contributed equally to this work.

Abstract

Objectives: **Gastric-type adenocarcinoma (GAS), an aggressive subtype of non-human papillomavirus (HPV)-associated (NHPVA) cervical adenocarcinomas (ADC), remains a treatment-refractory disease with poor prognosis. This study aims to explore the oncogenic mechanism and efficacious therapeutic target of GAS.**

Methods: **We included 19 NHPVA and 153 HPVA ADC patients from our center to investigate clinicopathological features. We collected 3 GAS and 2 usual-type endocervical adenocarcinomas (UEA) for single-cell RNA sequencing and T-cell receptor sequencing. We conducted immunohistochemical staining of 25 GAS and 25 UEA samples and multicolor immunohistochemical staining of 2 GAS samples for validation. We explored the efficacy of anti-clusterin (OGX-011) and/or cisplatin (DDP) for GAS based on GAS-derived tumoroids.**

Results: **Based on clinical data, we clinicopathologically verified the malignancy of GAS. Through single-cell RNA sequencing, we delineated key cell subtypes including GAS epithelial cells, "GAS-enriched fibroblasts", "GAS-associated $\gamma\delta$T cells", and CD8+ exhausted T cells enduring heat stress and contributing to GAS aggressive phenotype. Regarding validation, we verified clusterin (CLU)-associated heat stress, highlighted the potential role of CLU-associated stress in promoting immune escape, and established a four-gene signature (*CLU*, *PDGFB*, *TIGIT*, and *C3*) indicating poor prognosis of GAS induced by CLU-associated stress and immune escape. Based on GAS-derived tumoroids retaining the histological features, CLU-associated stress, and genetic profile of parental tumor, we validated the anti-tumor and sensitizing DDP efficacy of targeting CLU.**

Conclusion: **CLU-associated heat stress of key cell subtypes contributed to the malignant GAS microenvironment. Additionally, we pioneeringly constructed GAS-derived tumoroids and suggested that combining CLU-targeted treatment and DDP could improve the therapeutic efficacy for GAS.**

Keywords: cervical gastric-type adenocarcinoma, precise treatment, tumoroid model, scRNA-seq, TCR-seq

---

Received: 28 October 2025. **Revised:** 25 January 2026. **Accepted:** 3 February 2026

Graphical abstract

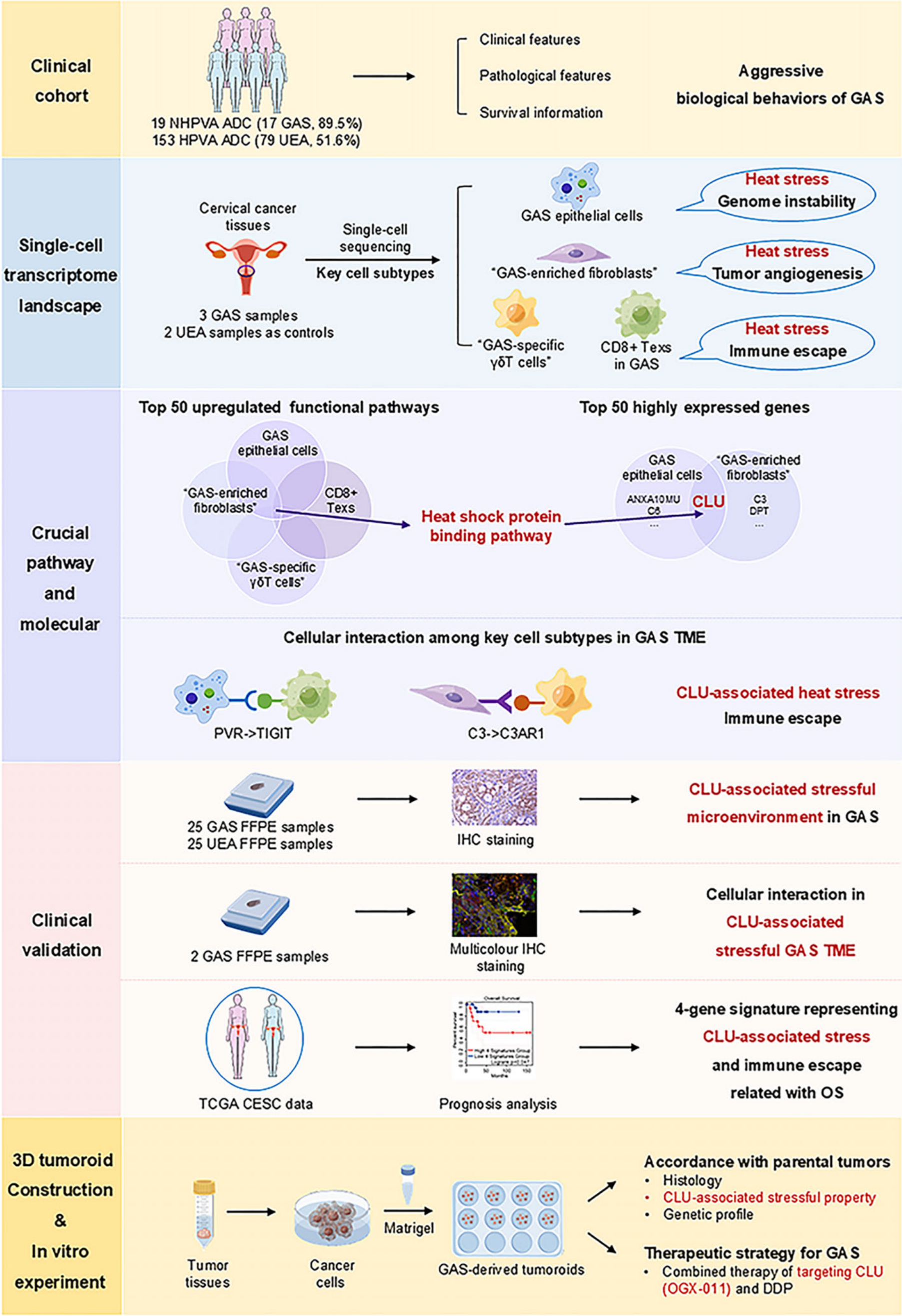

Schematic diagram of this study demonstrating unique CLU-associated stressful GAS TME and novel potential targets for precise treatment of GAS.

Introduction

Cervical cancer (CC) is the most prevalent cancer of the female reproductive system worldwide [1]. Compared to patients with squamous cell carcinoma, those with adenocarcinoma of the cervix (ADC) have a much poorer prognosis and higher mortality. According to the International Endocervical Adenocarcinoma Criteria and Classification proposed in 2018 [2], ADC can be classified into human papillomavirus (HPV)-associated (HPVA) and non-HPV-associated (NHPVA) ADC. Among NHPVA ADCs, gastric-type adenocarcinoma (GAS), which accounts for the greatest percentage (71%–87.5%), has received extensive attention given its high mortality and remarkable aggressiveness [3–5].

To date, the following challenges remain in the diagnosis and treatment of GAS. (i) High misdiagnosis rate: occurrence in the upper segment of the cervical canal, negative HPV infection testing results, and morphological traits similar to benign lesions make GAS easier to misdiagnose [6–8]. (ii) Remarkable aggressiveness: compared to usual-type endocervical adenocarcinoma (UEA), GAS is prone to not only vaginal and parametrial invasion but also appendage, peritoneum, and abdominal cavity metastases [9, 10]. (iii) Low treatment efficacy: the effectiveness of conventional radiotherapy, chemotherapy, and concurrent chemoradiotherapy (CCRT) is poor for patients with GAS, regardless of clinical stage [11]. It has been reported that the response rate of GAS to radiotherapy is lower than that of UEA (50% versus 81.8%) [10]. (iv) High recurrence rate and poor prognosis: recurrence of GAS occurs in up to 32% of patients, four times the recurrence rate of UEA [9]. Even at an early stage, GAS has an unfavourable prognosis. The 5-year overall survival (OS) was 36.9% for GAS versus 90.0% for HPVA ADC [9], whereas disease-specific survival was 42% for GAS versus 91% for HPVA ADC [12]. Briefly, it remains a great challenge to make a correct diagnosis and conduct effective therapeutic measures for GAS patients. One significant reason for such unsatisfactory clinical outcomes is inadequate understanding of the oncogenesis of GAS. Current studies have unilaterally focused on the carcinogenesis of GAS from a genomic perspective [13, 14], but are insufficient to comprehensively illustrate the pathogenetic mechanisms behind the malignant behaviors and poor prognosis of GAS. Hence, there is an urgent need for a more systematic and deeper exploration of the mechanisms underlying the aggressive characteristics of GAS.

It has been reported that the tumor-reprogrammed microenvironment plays a vital role in nurturing immune evasion, drug resistance, and tumor development [15, 16]. Recently, the combination of single-cell RNA sequencing (scRNA-seq) and T-cell receptor sequencing (TCR-seq) has provided an effective way to analyse the highly complex tumor microenvironment (TME), to detect key cellular subpopulations and intercellular crosstalk, and to explore the crucial pathways and molecular events within the TME [17–19]. Additionally, advances in tumoroid-based *in vitro* models, which have been defined as organ miniatures or avatars resembling tumour complexity [20], could aid our understanding of the role played by TME in cancer progression and its response to drug treatment, helping to guide personalized therapy. Currently, the consolidation of advanced methods has been applied in multiple cancers, not only providing insights into the mechanism of tumor progression but also facilitating novel therapeutic targets [21–23]. However, to our knowledge, no study has been published concentrating on the pathogenic mechanisms of GAS from the perspective of TME, integrating scRNA-seq and TCR-seq with a patient-derived tumoroid model, driving us to conduct further investigation.

In the present study, we first confirmed the aggressive phenotype and poor prognosis of GAS using clinical data from our center. Subsequently, we not only unveiled the unique clusterin (CLU)-associated heat stress in the GAS TME, but also demonstrated its potential role in promoting immunosuppression, collectively contributing to the malignancy of GAS. Most importantly, we innovatively established 3D GAS-derived tumoroids recapitulating the histological features, CLU-associated stressful TME, and genetic characteristics of the original tissue, and further validated the therapeutic efficacy and chemotherapy-sensitizing properties of targeting CLU by OGX-011, offering a novel research model for GAS and providing an encouraging outlook of targeting CLU for GAS treatment.

Materials and methods

Study population

We included 172 ADC patients from the Obstetrics and Gynaecology Hospital of Fudan University, including patients with HPVA ADC ($n = 153$) and NHPVA ADC ($n = 19$). The inclusion criteria were as follows: (i) hospitalized at our hospital for surgery from 1 July 2020 to 30 June 2021; (ii) diagnosis of adenocarcinoma or adenosquamous carcinoma of the cervix confirmed by pathological examination; and (iii) International Federation of Gynecology and Obstetrics (FIGO) clinical stage IA1-IIA2 based on preoperative diagnosis. The exclusion criteria were as follows: (i) pregnancy status or combination of other malignancies or severe medical or surgical disease; (ii) having received treatment (e.g. neoadjuvant chemotherapy) prior to undergoing surgical treatment for cervical cancer; (iii) death due to surgical complications; and (iv) excessive missing clinical information.

Data collection

We retrospectively collected the following clinical data from each patient: (i) clinical features: signs and symptoms (vaginal drainage, barrel cervix) and clinical tests [HPV test and liquid-based cytology test (LCT)], (ii) pathological features: histological subtypes (UEA, adenosquamous carcinoma, squamous carcinoma combined with adenocarcinoma, mucinous adenocarcinoma, minimal derived adenocarcinoma, and GAS) and pathological characteristics (infiltration depth, vaginal involvement, uterine involvement, adnexal invasion, and pelvic lymph node metastasis), and (iii) survival information: OS and regression-free survival (RFS).

The primary outcomes were 2-year RFS and 2-year OS. RFS was defined as the time interval from the initial ADC diagnosis to the first detection of any recurrence or the last follow-up. OS was defined as the time interval from the initial diagnosis to ADC-related death or the last follow-up. Patients who failed to achieve a survival event at the last follow-up were reviewed. Median OS was defined as the median time from the commencement of treatment until death from any cause. A significance level of 0.05 was used for all comparisons.

Human specimens

We included 3 GAS and 2 UEA samples for scRNA-seq and TCR-seq. Immunohistochemical (IHC) staining was performed on 25 UEA and 25 GAS samples, and multicolor immunohistochemical (mIHC) staining was performed on 2 GAS samples. GAS-derived tumoroids were established from another 1 case of GAS. All of the included tumor samples were obtained during primary treatment of surgical resection. Detailed clinical characteristics of GAS and UEA samples are shown in supplementary Tables 1, 2, 3, and 4, see online supplementary material.

scRNA-seq and TCR-seq

Utilizing the 10 × Genomics Chromium Controller Instrument, Chromium Single Cell 5’ library, gel bead kit, and V(D)J enrichment kit (10 × Genotics, Pleasanton, CA, USA), scRNA-seq and TCR-seq libraries were prepared. scRNA-seq was conducted by professionals from NovelBio Co, Ltd. Briefly, cells were concentrated to 1000 cells/μl and loaded into each lane to produce single-cell gel bead-in-emulsions (GEMs), yielding an expected 5000 single-cell mRNA barcodes per sample. Following the reverse transcription step, the GEMs were disrupted, and the barcoded cDNA was purified and amplified. This amplified barcode cDNA was then utilized to construct 5’ gene-expression libraries and TCR enrichment libraries. For the construction of 5’ libraries, the amplified barcode cDNA was fragmented, A-tailed, ligated with an articulator, and amplified using exponential PCR. For V(D)J libraries, human T-cell V(D)J sequences were enriched from the amplified cDNA, followed by fragmentation, A-tailing, articulator ligation, and exponential PCR amplification. The final libraries were quantified using the Qubit high-sensitivity DNA assay (Thermo Fisher Scientific), while the size distribution of the libraries was determined using a high-sensitivity DNA microarray on a Bioanalyzer 2200 (Agilent). All the libraries were sequenced by Illumina sequencing (Illumina, San Diego, CA, USA) with 150 bp paired-end sequences.

Gene ontology analysis

Gene ontology (GO) [24] analysis was performed to facilitate the elucidation of the biological significance of marker genes and differentially expressed genes (DEGs). We downloaded GO annotations (http://www.ncbi.nlm.nih.gov/), UniProt (http://www.uniprot.org/), and GO (http://www.geneontology.org/) from National Center for Biotechnology Information (NCBI). Fisher’s exact test was used to identify significant GO categories, and FDR was used to correct for P values.

Pathway analysis

Based on the Kyoto Encyclopedia of Genes and Genomes (KEGG) database, significant pathways for marker genes and DEGs were identified using pathway analysis. We turned to Fisher’s exact test to select significant pathways, with significance thresholds defined by *P* values and false discovery rates (FDRs) [25].

Pseudotime analysis

We applied a single-cell trajectory analysis (http://cole-trapnell-lab.github.io/monocle-release) using Monocle2 along with the discriminative dimensionality reduction (DDR) tree and default parameters. Prior to the Monocle analysis, we selected Seurat clustering results for marker genes and passed raw expression counts of filtered cells. The branching expression analysis model (BEAM analysis) was applied to the gene analysis for branching fate determination based on pseudotemporal analysis.

CytoTRACE

Cellular Trajectory Reconstruction Analysis using gene Counts and Expression (CytoTRACE), a computational method, was applied to predict the differentiation state of cells from scRNA-seq data by counting the number of detectably expressed genes per cell [26].

Cell communication analysis

To make possible a systematic analysis of cell–cell communication molecules, we applied cell communication analysis based on CellPhoneDB [27], a public repository of ligands, receptors, and their interactions. Membrane proteins, secreted proteins, and peripheral proteins were annotated for clusters at different time points. Significant mean and cell communication significance (P value < 0.05) were calculated based on the interactions obtained by Seurat normalization and the normalized cell matrix.

QuSAGE analysis (gene enrichment analysis)

To characterize the relative activation of a given gene set, such as the KEGG, Hallmark (h.all.v7.0.symbols, https://www.gsea-msigdb.org/gsea/msigdb/index.jsp), and Reactome (https://reactome.org) gene sets, QuSAGE (2.16.1) analysis was performed [28].

Differential gene expression analysis

To identify DEGs between samples, FindMarkers, a function with the Wilcoxon rank sum test algorithm, was used under the following criteria: (i) Logarithm of Fold Change (lnFC) > 0.25; (ii) P value < 0.05; and (iii) minimum pressure > 0.1.

TCGA public dataset analysis

We downloaded clinicopathological information, and survival data of the TCGA CESC dataset from Xena (https://xenabrowser.net/datapages/). Survival analysis was conducted using the powerful online tool GEPIA (http://gepia.cancer-pku.cn/) or R software (version 3.6.2; R Foundation for Statistical Computing) with packages.

Cell culture

HT-3 cells were maintained in Dulbecco’s modified Eagle’s medium (Gibco, 11 965 118) containing 10% fetal bovine serum and 1% penicillin streptomycin. Cells between passages 10–20 were used for experiments following authentication by short tandem repeat (STR) profiling. Routine mycoplasma testing was performed using the MycoAlert detection kit (Lonza, LT07-218).

In vitro cytotoxicity assay

The cytotoxicity under different treatment conditions was assessed using the cell counting kit-8 (CCK8) assay. Cells were seeded into culture plates and exposed to various drug treatments, including cisplatin (DDP), CLU inhibitor (OGX-011), and their combination. Cell viability was evaluated by CCK-8 assay 72 h after transfection. Cell viability was measured according to the manufacturer’s instructions using the CCK8 assay, with absorbance recorded at 450 nm on a microplate reader. The viability of cells is calculated as $(As-Ab)/(Ac-Ab) \times 100\%$ (As: treated groups; Ab: blank; Ac: control).

RNA isolation, reverse transcription, and quantitative real-time PCR

Total RNA was isolated with Trizol reagent (Invitrogen, #15596026) and reverse transcribed using first-strand cDNA synthesis supermix (YEASEN, #11141ES60). Quantitative PCR was performed on a Step One Plus Real-Time PCR System with SYBR green mix (YEASEN, #11203ES08), using β-actin as endogenous control. *CLU* expression was calculated by the $2^{-\Delta\Delta Ct}$ method with triplicate technical replicates.

Western blotting

Proteins were extracted using either western/immuno precipitation (IP) lysis buffer or RIPA buffer containing protease/phosphatase inhibitors. Protein concentration was determined by bicinchoninic acid assay. Samples were separated by sodium dodecyl sulfate–polyacrylamide gel electrophoresis (SDS-PAGE) and transferred to polyvinylidene fluoride (PVDF) membranes (0.45 μm) using a Bio-Rad system. After blocking with 5% bovine serum albumin for 1 h, membranes were incubated with primary antibodies at 4°C overnight, followed by incubation with secondary antibodies at room temperature for 1 h. Protein bands were visualized by enhanced chemiluminescence detection (ImageQuant LAS 4000) and quantified using ImageJ.

GAS-derived tumoroid culture

After isolating, the GAS tissues (supplementary Table 4) were placed in sterile phosphate-buffered saline (PBS) and transported to the laboratory, maintaining a temperature of 4°C. To minimize contamination, the tissues were submerged in 20 ml of pre-cooled (4°C) PBS containing a 2 × solution of penicillin/streptomycin/amphotericin B (Solarbio, Cat#P7630, Beijing, China) under sterile conditions for 5 min. They were then washed three times with the same solution. Following each wash, the tube containing the tissues was chilled on ice to allow natural sedimentation, and as much supernatant was removed as possible to eliminate impurities. Subsequently, the tissue was cut into small pieces using ophthalmic scissors, aiming for a size of 0.5–1 mm^2 (excessive fragmentation could affect cell viability). Next, an appropriate amount of GAS tissue dissociation solution was added, consisting of 2 mg ml^{-1} of collagenase I (Solarbio, Cat#C8140, Beijing, China), 2 mg ml^{-1} of dispase II (Solarbio, Cat#D6430, Beijing, China), and 0.2 mg ml^{-1} of DNase I (Solarbio, Cat#D8071, Beijing, China) in Dulbecco's modified Eagle's medium (BOSTER, Cat#PYG0004, Shanghai, China). This medium was supplemented with 1 × penicillin/streptomycin (Solarbio, Cat#P1400, Beijing, China) and 10 μm Y-27632 (MCE, Cat#HY-10583, Shanghai, China). The tissue pieces were then digested at 37°C for 40–60 min. During this digestion process, the fragments were mixed with the collagenase I solution every 10 min, and the progress of digestion was monitored. Once digestion was complete, the cells were filtered through a 70 μm nylon cell strainer and centrifuged for 5 min at 400 × g. If a visible red color was present in the cell pellet, 5 ml of red blood cell lysis buffer (Standard Reagent, Cat#0 210 706, Hyderabad, India) was added to remove red blood cells. The resulting cells were then embedded into basement membrane matrix (M001-04, Jiyan bio tech, Shanghai, China) on suspension plates and covered with the full growth medium.

At 2 days prior to drug exposure, organoids were disrupted into single cells using TrypLE and filtered using a 70-mm nylon cell strainer. A total of 2000 cells were seeded in 96-well plates and allowed to form organoids for 5 days. Cisplatin (5 μm) (MCE, Cat#HY-17394, Shanghai, China) and 300 nm OGX-011 (MCE, Cat#HY-143230, Shanghai, China) were added. Cisplatin and OGX-011 were dissolved in PBS. All wells were normalized to the solvent used. Images were captured using a Leica SP8 confocal microscope at 0 day (0 h), 1 day (24 h), 2 days (48 h), and 3 days (72 h) after drug addition. Three selected fields of images were captured in each sample, and the sizes of tumoroids were estimated using ImageJ.

IHC analysis

Overall, 25 GAS and 25 UEA tissues from human models were collected and fixed in 10% formalin overnight and embedded in paraffin (supplementary Table 2). A list of antibodies used in this study is provided in supplementary Table 5, see online supplementary material. Integrated optical density (IOD) was measured using Image-Pro Plus according to a previous study [29]. Average optical density (AOD), which was calculated by dividing IOD by area, reflects the expression level of the target protein. Using median H-score as the cutoff, patients were classified into high- or low-TIGIT groups or high- or low-C3 groups ($n = 25$ each).

Immunofluorescence staining and histological processing

GAS-derived tumoroids were collected and suspended in 4% paraformaldehyde (PFA) at room temperature for 1 h for fixation and then washed in PBS and cryoprotected in 15% sucrose in PBS for 4–5 h followed by 30% sucrose overnight at 4°C. GAS-derived tumoroids were embedded together in blocks in tissue-freezing medium, frozen on dry ice, and stored at −70°C. Then, 10–30 μm cryosections of tumoroids were obtained and stored at −70°C.

Immunofluorescence staining was performed as previously described [30]. Slides were thawed, dried for 5–10 min in a 37°C incubator, rehydrated in PBS for 5 min, and blocked and permeabilized in blocking solution (5% normal donkey serum, 0.1% Triton X-100 in PBS). The tissue area and slide edges were outlined using a hydrophobic PAP pen (Abcam, ab2601, Shanghai, China), and then slides were incubated with ∼500 ml of blocking/permeabilization solution (0.1% Triton-X, 5% normal donkey serum in PBS) in a humidified chamber for 1 h at room temperature. Slides were incubated in the appropriate primary antibody diluted in blocking solution under parafilm at 4°C overnight. Sections were washed in PBST (0.05% Tween in PBS), incubated with appropriate fluorochrome-conjugated secondary antibodies diluted in blocking solution at room termperature for 1 h in the dark, washed twice in PBS, counterstained with 4',6-diamidino-2-phenylindole (DAPI) (1 μg/ml, Sigma–Aldrich, MO, USA) for 5 min, and rinsed twice in PBS. All images were collected using a Leica SP8 confocal microscope and analysed using ImageJ software. A list of antibodies used in this study is provided in supplementary Table 5.

mIHC analysis

mIHC staining was performed on 2 formalin-fixed, paraffin-embedded (FFPE) GAS samples (supplementary Table 3) by staining 4-μm-thick FFPE whole-tissue sections with standard primary antibodies sequentially and pairing with a tyramide signal amplification (TSA) 6-color kit (abs50015-100T, Absinbio, Shanghai, China). Then, the cells were stained with DAPI. For example, deparaffinized slides were incubated with anti-COL1A1 antibody (#72026T, CST, MA, USA) for 30 min and then treated with anti-rabbit/mouse horseradish peroxidase-conjugated secondary antibody (abs50015-02, Absinbio, Shanghai, China) for 10 min. Then, labelling was developed for a strictly observed 10 min using TSA 570 as per the manufacturer's direction. Slides were washed in TBST buffer and then transferred to preheated citrate solution (90°C) before being heat-treated using a microwave set at 20% of maximum power for 15 min. Slides were cooled in the same solution to room temperature. Between all steps, the slides were washed with Tris buffer. The same process was repeated for the antibodies/fluorescent dyes. Each slide was then treated with two drops of DAPI (abs47047616, Absinbio, Shanghai, China), washed in distilled water, and manually coverslipped. Slides were air dried, and pictures were taken with Pannoramic MIDI II (3DHISTECH, Budapest, Hungary). Images were analysed using Indica Halo software.

Whole genome sequencing

Whole genome sequencing (WGS) was performed for one tumor tissue and one tumoroid (Supplementary Table 4). WGS libraries were prepared with the TruSeq PCR free library prep kit and 150 bp paired-end sequences were generated on a NovaSeq 6000 or HiSeqX instrument with a median of 100 × coverage (Illumina, San Diego, CA). The Illumina WGS pipeline (version 5.0) and tumor-normal app (version 3.0) were used for variant calling of small nucleotide variants and structural variants. In brief, WGS reads were mapped to a human reference genome (GRCh37) using Isaac aligner [31] (version 03.16.02.19). Structural variants were then called using Manta caller [32] (version 0.28.0). Single nucleotide variants and small indels (SNVs) were called using Strelka software [33] (version 2.4.7). The tumor-normal app used a mixture of genomic DNA from multiple anonymous donors as unmatched-normal controls. To remove potential germline variants, all SNVs with PASS flag were queried against the gnomAD database (https://gnomad.broadinstitute.org/) and variants with global population frequencies > 1% where excluded.

Statistical analysis

In the Results section and figure legends, specific statistical tests and metrics are outlined, including mean ± SD or median values with 95% confidence intervals, along with sample sizes. For comparing continuous data of varying types between two groups, we employed the unpaired two-tailed Student's t-test. For comparing data across multiple groups, one-way ANOVA with Tukey's *post hoc* test was utilized. All statistical analyses were conducted using GraphPad Prism version 8 (GraphPad Software, La Jolla, CA, USA). The predict receiver operating characteristic (ROC) model curve was used to evaluate the sensitivity and specificity of CLU as a biomarker. The threshold for statistical significance was set at $P < 0.05$.

Results

Clinical cohort: GAS accounting for 89.5% of NHPVA ADC cases showed an aggressive phenotype and poor prognosis

To explore the unique clinicopathological features and prognostic characteristics of NHPVA ADC, especially GAS, we retrospectively collected clinical data from 172 patients from our center; 19 patients had NHPVA ADC, 89.5% of which were GAS; of the remaining 153 cases of HPVA ADC, UEA accounted for 51.6%. The study selection schematic diagram is presented in Fig. 1A and the clinicopathological characteristics are summarized in Table 1. (i) We found that patients with NHPVA ADC were more likely to be misdiagnosed even if they underwent screening programs (HPV test combined with LCT) ($P < 0.001$), indicating the difficulty in making a correct and timely diagnosis. (ii) Regarding clinical features, patients with NHPVA ADC had a higher rate of vaginal drainage (57.9% versus 17.6%, $P < 0.001$) and barrel cervix (36.8% versus 11.8%, $P = 0.009$), revealing unique properties and morphology. (iii) NHPVA ADC exhibited more malignant biological behavior than HPVA ADC, namely deeper stromal infiltration (94.7% versus 41.8%, $P < 0.001$) and a greater tendency to spread and metastasize, including vaginal involvement (52.6% versus 20.9%, $P = 0.008$), uterine body involvement (68.4% versus 18.3%, $P < 0.001$), adnexal involvement (21.1% versus 2.6%, $P = 0.006$), and pelvic lymph node metastasis (57.9% versus 19.6%, $P < 0.001$). (iv) NHPVA ADC patients showed a worse prognosis in terms of both OS ($P = 0.0013$) and RFS ($P = 0.0048$) than HPVA ADC patients (supplementary Fig. 1, see online supplementary material). In brief, NHPVA ADC, of which GAS accounted for 89.5% of cases, exhibited more aggressive phenotype and poorer prognosis.

Given that GAS, the most common subtype of NHPVA ADC, showed such aggressive clinical features, we next investigated the microenvironment of GAS to unveil the underlying molecular events.

Single-cell transcriptome landscape: GAS TME showed distinct cell composition regarding epithelial cells, fibroblasts, and T cells

To explore the TME of GAS, scRNA-seq was applied to 3 GAS samples and 2 UEA samples as controls (Fig. 1B). After data preprocessing and quality control, a total of 22 844 cells were differentiated into 21 different clusters (clusters 0–20) through principal component analysis and partitioned into eight major groups (Fig. 1C and D) annotated by well-known cell-type markers (Fig. 1E): T cells (*CD2*, *CD3D*, and *CD3E*), B cells (*CD19*, *CD79A*, and *MS4A1*), plasma cells (*IGHG1*), myeloid cells (*CD14* and *C1QA*), fibroblasts (*DCN*, *COL1A1*, and *TAGLN*), endothelial cells (*PECAM1* and *VWF*), epithelial cells (*EPCAM*, *KRT18*, and *KRT8*), and undefined cells (*PTPRC* and *CD79A*-negative). Additionally, we presented the cell atlas in

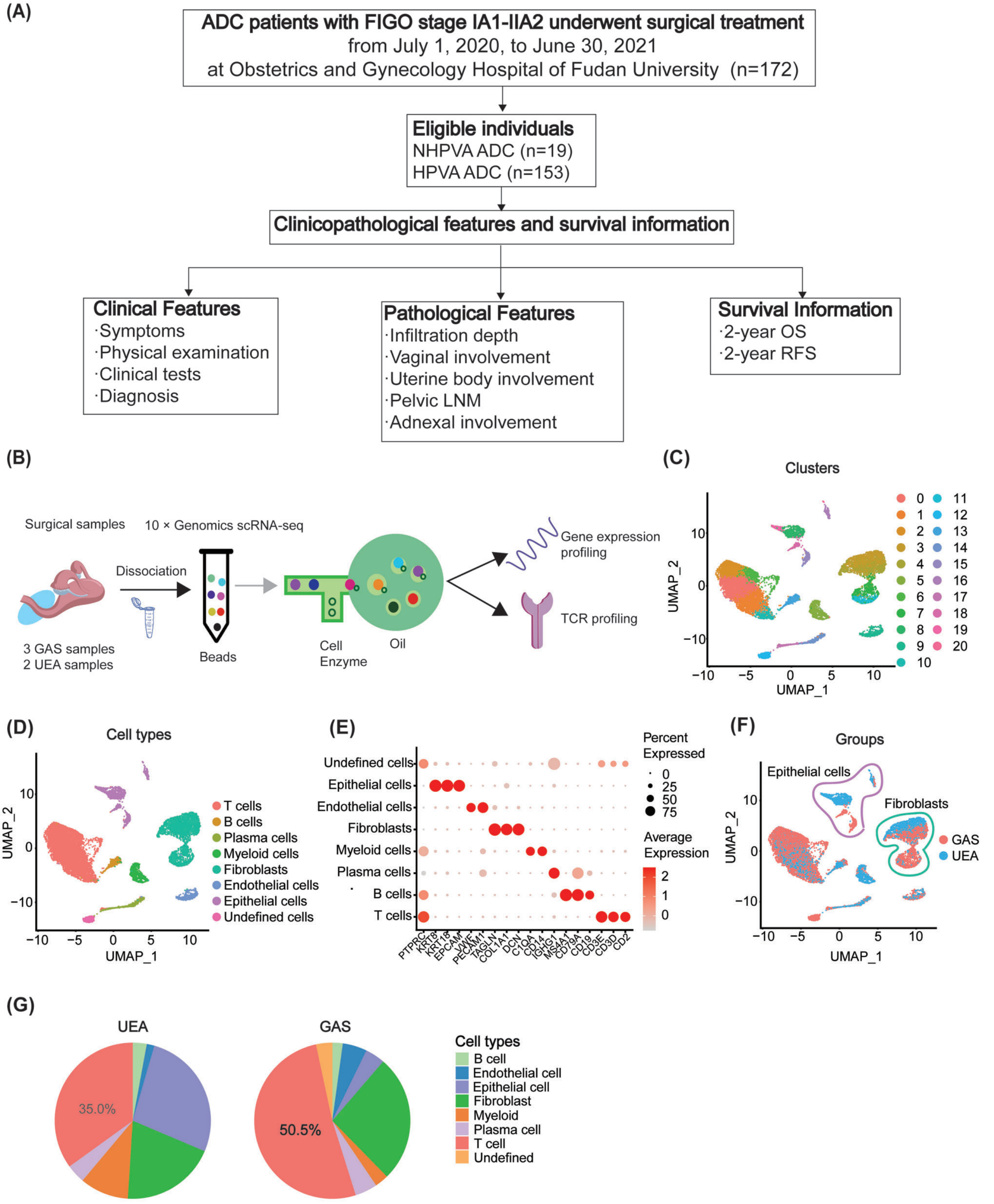

Figure 1 Flowchart of the clinical data analysis and single-cell transcriptome atlas of GAS and UEA as control. (**A**) Flowchart of the clinical data analysis for the comparison of clinical features between HPVA and NHPVA patients. (**B**) Schematic diagram of scRNA-seq and TCR-seq of 3 GAS samples and 2 UEA samples. (**C**) UMAP plots demonstrating 22 844 cells reclustered into 21 clusters. (**D**) UMAP plots demonstrating 21 clusters further categorized into eight major cell types. (**E**) Bubble plots showing marker gene expression in eight major cell types. The colors represent the average expression levels, and dot sizes represent the percentage expression of selected genes. (**F**) UMAP plots of all the cells presenting in different histological groups, including UEA and GAS. Each dot corresponds to a single cell colored according to different groups, including UEA and GAS. Epithelial cells and fibroblasts from GAS and UEA did not aggregate with each other, showing significant heterogeneity in UEA and GAS. (**G**) Pie plot indicating the different ratios of cell subtypes between UEA and GAS. Strikingly, T cells were more abundant in GAS.

Table 1 Comparison of the clinicopathological features between HPVA and NHPVA ADC.

Clinicopathological features		HPVA ($n = 153$)	NHPVA ($n = 19$)	P value
Pathological subtypes				
	UEA	79 (51.6%)	0	/
	Adenosquamous carcinoma	68 (44.4%)	0	
	Squamous carcinoma combined with adenocarcinoma	5 (3.3%)	0	
	Mucinous adenocarcinoma	1 (0.7%)	0	
	Minimal deviation adenocarcinoma	0	2 (10.5%)	
	GAS	0	17 (89.5%)	
HPV infection				
	Positive	135 (88.2%)	2 (15.0%)	<0.001
	Negative	3 (2.0%)	14 (70.0%)	
	Unknown	15 (9.8%)	3 (15.0%)	
LCT				
	Negative for intraepithelial lesion or malignancy (NILM) and benign changes	30 (19.6%)	8 (42.10%)	0.015
	Pathological changes	84 (54.9%)	4 (21.1%)	
	Unknown	39 (25.5%)	7 (36.8%)	
HPV-LCT screening double negative				
	Yes	1 (0.7%)	6 (31.6%)	<0.001
	No	140 (91.5%)	10 (52.6%)	
	Unknown	12 (7.8%)	3 (15.8%)	
Clinical features				
	Vaginal drainage	27 (17.6%)	11 (57.9%)	<0.001
	Barrel cervix	18 (11.8%)	7 (36.8%)	0.009
Pathological features				
	Infiltration depth (1/3 to full depth)	64 (41.8%)	18 (94.7%)	<0.001
	Vaginal involvement	32 (20.9%)	10 (52.6%)	0.008
	Uterine body involvement	28 (18.3%)	13 (68.4%)	<0.001
	Adnexal involvement	4 (2.6%)	4 (21.1%)	0.006
	Pelvic lymph node metastasis	30 (19.6%)	11 (57.9%)	<0.001

different histological subtypes, including GAS and UEA (Fig. 1F). In particular, we found that epithelial cells and fibroblasts from GAS and UEA samples did not aggregate with each other (Fig. 1D and F), illustrating that epithelial cells and fibroblasts in GAS were basically distinct from those in UEA. In addition, we noticed that T cells were more numerous in GAS (Fig. 1G).

Given that epithelial cells, fibroblasts, and T cells from GAS showed remarkable heterogeneity compared with those in UEA, we hypothesized them as significant players in GAS TME. Thus we further explored the unique features and functions of these cell types in the microenvironment of GAS.

Key cell subtypes in GAS TME: epithelial cells, fibroblasts, and T cells in GAS endured heat stress and potentially contributed to aggressive phenotype of GAS

GAS epithelial cells endured heat stress and presented genome instability

Considering that epithelial cells play a decisive role in oncogenesis [34] and GAS epithelial cells were notably distinct from UEA ones, we first focused on GAS epithelial cells to explore their unique features. Based on unsupervised reclustering, we identified eight subclusters of epithelial cells (Fig. 2A). Among them, epithelial cells in subclusters 2 and 4 were derived from GAS samples, whereas epithelial cells in subclusters 0, 1, 3, 5, 6 and 7 were derived from UEA samples (Fig. 2B). Firstly, functional enrichment pathway analysis revealed that GAS epithelial cells were actively involved in regulation of cellular response to heat (Fig. 2C), implying heat stress of GAS epithelial cells. Besides, regarding genome variation, we found that classic mutated genes previously reported in GAS, including *STK11*, *TP53*, *PAX8*, and *KRT20* [35], were expressed at low levels in GAS epithelial cells (Fig. 2D), potentially revealing genome instability of GAS epithelial cells. Through inferred copy number variation (inferCNV) analysis, the average copy number variation (CNV) of GAS epithelial cells was the highest among all of the cell subtypes in GAS TME (Fig. 2E), suggesting the significant role of GAS epithelial cells in contributing to the highly malignant phenotype of GAS. Furthermore, the average CNV of GAS epithelial cells was higher than that of UEA ones (Fig. 2E), highlighting greater genome instability and higher malignancy of GAS epithelial cells compared to UEA ones. Collectively, GAS epithelial cells might endure heat stress and present genome instability, potentially contributing to the malignant phenotype of GAS.

"GAS-enriched fibroblasts" with heat stress exhibited tumor angiogenesis

Given that fibroblasts play instrumental roles in matrix remodeling to shape the TME [36] and GAS fibroblasts showed remarkable heterogeneity from UEA ones, we subsequently investigated their characteristics. Through unsupervised reclustering and annotation of fibroblasts, 11 subclusters were identified and five subgroups were categorized, including smooth muscle cells (SMCs) (subcluster 10; *DES* and *MYH11*), m-pericytes (subcluster 4 and 5; *RERGL* and *CRIP1*), f-pericytes (subcluster 9; *STEAP4* and *ITGA1*), myoblastic cancer-associated fibroblasts (myCAFs; subcluster 0, 2, 3, 6, and 8; *SOX4* and *IGFBP5*), and inflammatory CAFs (iCAFs; subcluster 1 and 7; *C3* and *DPT*) (Fig. 2F, G, and H). Remarkably, given that the infiltration abundance of iCAFs, m-pericytes and SMCs was significantly higher in GAS than in UEA (Fig. 2I), we classified iCAFs, m-pericytes, and SMCs as "GAS-enriched fibroblasts". Based on marker gene expression and functional pathway enrichment analysis, we discovered that "GAS-enriched fibroblasts" participated in angiogenesis highly expressing associated genes (*VEGFB*, *CCN2* and *CCN1*) and were involved in cellular response to heat highly expressing heat stress-related genes (*PDGFB*, *HSPB1*, and *HSP90AA1*) (Fig. 2J, K, and L), highlighting the proangiogenic effects of "GAS-enriched fibroblasts" with great heat stress, potentially promoting GAS progression.

T cells in GAS played vital roles in immune escape with great heat stress load in GAS TME

"GAS-associated $\gamma\delta$T cells" in GAS with heavy heat stress load revealed immune dysfunction

Given that T cells play vital roles in antitumor immunity and are highly abundant in the GAS TME, we next explored their specific characteristics. In addition to well-recognized CD4+ T cells and CD8+ T cells, we discovered a group of $\gamma\delta$ T cells whose roles in GAS tumorigenesis are poorly understood. Through unsupervised reclustering, three subsets of $\gamma\delta$ T cells were identified, including $\gamma\delta$T_ITGAE (subcluster 0; *ITGAE*, *TRDV1*, *CLIC3*), $\gamma\delta$T_AREG (subcluster 1; *AREG*, *LTB*, *IL7R*), and $\gamma\delta$T_NKG7 (subcluster 2; *NKG7*, *LAG3*, *GNLY*) (Fig. 3A). Notably, given that $\gamma\delta$T_ITGAE cells were observed in both GAS and UEA TME, whereas $\gamma\delta$T_AREG and $\gamma\delta$T_NKG7 cells were only observed in the GAS microenvironment (Fig. 3B), we classified $\gamma\delta$T_AREG and $\gamma\delta$T_NKG7 cells as "GAS-associated $\gamma\delta$T cells" and further explored their characteristics. According to CytoTRACE and pseudotime analyses, we discovered that "GAS-associated $\gamma\delta$T cells" holding less differentiation diversity compared to $\gamma\delta$T_ITGAE cells, were at the final differentiation state (Fig. 3C and D). Along the developmental trajectory of $\gamma\delta$ T cells, we observed higher expression of heat stress-related genes (*XBP1*, *HSP90AB1*, *BAG3*) and immune checkpoint genes (*CTLA4*, *LAG3*, *TIGIT*) in "GAS-associated $\gamma\delta$T cells" (Fig. 3E), indicating the heat stress load and immune dysfunction in "GAS-associated $\gamma\delta$T cells". Besides, according to marker gene expression and functional enrichment pathway analysis, "GAS-associated $\gamma\delta$T cells" were characterized by not only the heat shock protein binding pathway (*BAG3*, *HSPD1*, *HSPE1*. and *HSP90AB1*) (Fig. 3F and H) but also the PD-1 checkpoint pathway in cancer (*LTB*, *LAG3*, *SERF2*, *PTPRCAP*. and *CD52*) (Fig. 3G and I), implying that "GAS-associated $\gamma\delta$T cells" exhibited accumulated heat stress load and immune dysfunction. Briefly, "GAS-associated $\gamma\delta$T cells" with accumulated heat stress load manifested immune dysfunction, contributing to the formation of the aggressive clinical phenotype of GAS.

CD8+ T cells especially CD8+ Texs in GAS with accumulation of heat stress showed immunosuppression

Considering that CD8+ T cells, as the major effector of adaptive immunity, have the ability to selectively detect and eradicate cancer cells [37], we next focused on CD8+ T cells to investigate the exact role of CD8+ T cells in GAS TIME. Based on unsupervised clustering, we classified CD8+ T cells into the four main groups: central memory T cells (Tcms; *GPR183* and *CCR7*); effector memory T cells (Tems; *GZMA* and *HLA-DRB1*), effector T cells (Teffs; *FGFBP2* and *FCGR3A*); exhausted T cells (Texs; *LAYN* and *CXCL13*) (Fig. 4A). Among them, Texs, which are seen as the main cause of poor tumor control [38], greatly interested us. According to DEG analysis and functional pathway analysis, we discovered that Texs were involved in heat shock protein binding highly expressing heat stress-related genes (*HSP90AA1*, *HSPE1*, *HSPD1*, *HSPB1*, and *DNAJA1*) (Fig. 4B and D) and PD-1 checkpoint pathway in cancer highly expressing immune checkpoint genes (*TIGIT*, *LAYN*, *CTLA4*, *PDCD1*, and *LAG3*) (Fig. 4C and E), indicating that CD8+ Texs endured heat stress and exhibited immune escape. Additionally, based on pseudotime analyses, CD8+ Texs were at the final state of differentiation (Fig. 4F). In addition, along the developmental trajectory of CD8+ T cells, we observed elevated expression of stress-related genes (*HSP90AA1*, *HSPD1*, and *HSPE1*) and immune checkpoint genes (*LAG3*, *LAYN*, and *TIGIT*) (Fig. 4G), implying the accumulated heat stress load and gradual immune dysfunction of Texs. Furthermore, the expression level of immune checkpoint genes (*LAG3*, *LAYN*, and *TIGIT*) was positively correlated with that of stress-related genes (*HSP90AA1*, *HSPD1*, and *HSPE1*) ($R = 0.66$, $P < 0.0001$) (Fig. 4H), indicating that immune dysfunction of CD8+ T cells was closely associated with heat stress accumulation. Remarkably, the infiltration abundance of Texs was higher in GAS than in UEA (Fig. 4I), whereas the expression levels of heat stress-related genes (HSPB1, BAG3, and ST13) and immune checkpoint genes (*CTLA4*, *TIGIT*, and *CD96*) were significantly higher in GAS Texs than those in UEA (Fig. 4J), demonstrating a higher extent of stress endurance and immune dysregulation of Texs in GAS, thus leading to greater disease aggressiveness of GAS. Besides, regarding clonotypic expansion through TCR-seq, we found that CD8+ Texs in GAS samples generally harbored a higher degree of expanded clonotypes than those in UEA samples, probably due to the activation of cancer neoantigens derived from genome instability in GAS, implying greater immune exhaustion in GAS (Fig. 4K). In short, CD8+ Texs in GAS, with notable accumulation of heat stress, manifested immune exhaustion with highly expanded clonotype, playing a role in promoting malignancy of GAS.

To summarize, key cell subtypes in GAS TME including genome-unstable GAS epithelial cells, proangiogenic "GAS-enriched fibroblasts", and immunosuppressed T cells in GAS ("GAS-associated $\gamma\delta$T cells" and CD8+ Texs in GAS) might endure heat stress and contribute to the formation of the malignant phenotype and immune dysfunction of GAS.

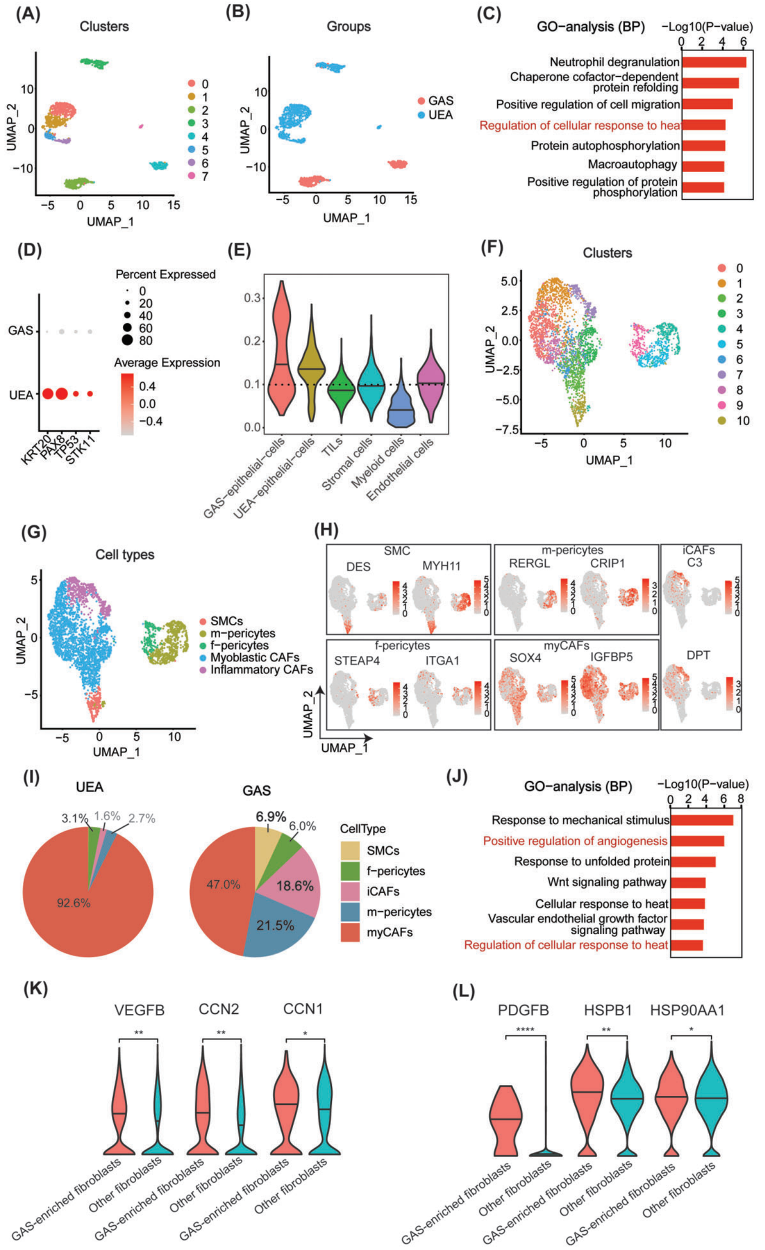

Figure 2 Genome unstable GAS epithelial cells and proangiogenic "GAS-enriched fibroblasts" endured heat stress in the GAS TME. (**A**) UMAP plot of eight epithelial cell subclusters generated from unsupervised reclustering. (**B**) UMAP plot of epithelial cells with different histological groups, including UEA and GAS samples, showed significant heterogeneity of epithelial cells between UEA and GAS. (**C**) Bar plot showing a high level of regulation of cellular response to heat through GO analysis in epithelial cells presented with statistical significance [$-\text{Log}_{10}(P \text{ value})$]. (**D**) Dot plot indicating the different expression levels and cell expression proportions of classic mutant genes previously reported in GAS, such as *STK11*, *TP53*, *PAX8*, and *KRT20* between GAS and UEA. The colors represent the average expression levels, and dot sizes represent the percentage expression of selected genes. (**E**) Violin plots showing distribution of copy number variation scores among different cell types from GAS and UEA indicating the most significant genome stability in epithelial cells, especially in GAS epithelial cells. (**F**) UMAP plots of the 11 subclusters generated from fibroblasts reclustering. (**G**) UMAP plots of the 11 subclusters of fibroblasts categorized into 5 subgroups including smooth muscle cells (SMCs), m-pericytes, f-pericytes, myoblastic cancer-associated fibroblasts (myCAFs) and inflammatory CAFs (iCAFs). (**H**) UMAP plots showed the expression levels of the specific marker genes for the 5 types of fibroblasts: *DES* and *MYH11* for SMCs, *RERGL* and *CRIP1* for m-pericytes, *STEAP4* and *ITGA1* for f-pericytes, *SOX4* and *IGFBP5* for myCAFs, and *C3* and *DPT* for iCAFs. The color key from grey to red indicates relative expression levels from low to high. (**I**) Pie plots showing the different ratios of each major cell type of fibroblasts in UEA and GAS, indicating that the infiltration abundance of iCAFs, m-pericytes and SMCs was much higher in GAS than in UEA and we classified iCAFs, m-pericytes and SMCs as "GAS-enriched fibroblasts". Moreover, we classified myCAFs and f-pericytes as other fibroblasts. (**J**) Bar chart showing the enrichment of positive regulation of angiogenesis and cellular response to heat based on the GO pathways in "GAS-enriched fibroblasts" presented with statistical significance [$-\text{Log}_{10}(P \text{ value})$]. (**K**) Violin plots indicating the higher expression level of genes associated with angiogenesis (*VEGFB*, *CCN2*, and *CCN1*) in "GAS-enriched fibroblasts" compared to other fibroblasts. *P* values were obtained by Student's t-test. $^{*}P < 0.05$; $^{**}P < 0.01$. (**L**) Violin plots indicating the higher expression level of genes associated with heat stress (*PDGFB*, *HSPB1*, and *HSP90AA1*) in "GAS-enriched fibroblasts" compared to other fibroblasts. *P* values were obtained by Student's t-test. $^{*}P < 0.05$; $^{**}P < 0.01$; $^{****}P < 0.0001$.

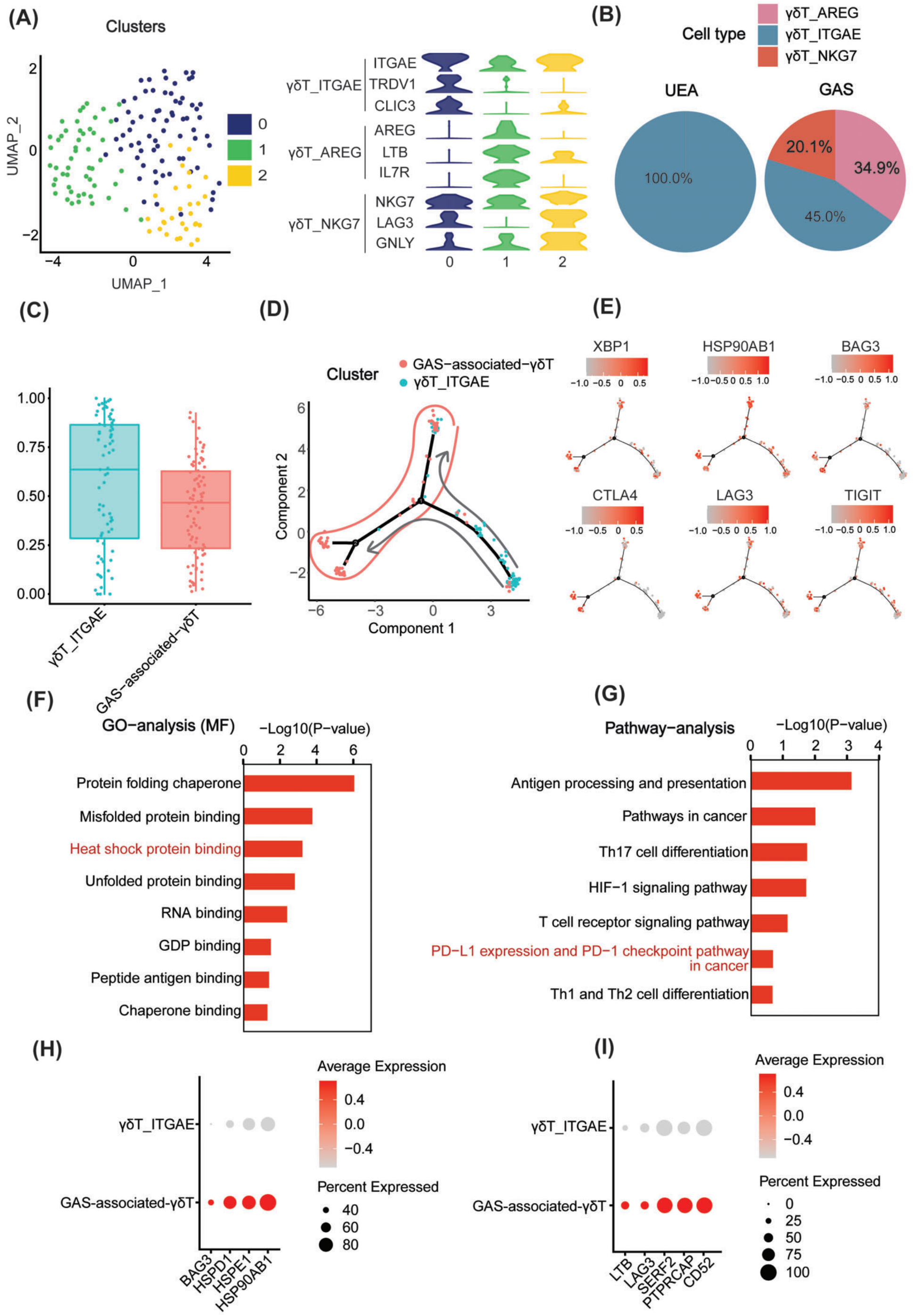

Figure 3 "GAS-associated $\gamma\delta$T cells" with heavy heat stress load revealed immune dysfunction in GAS TME. (**A**) UMAP plots of the three subclusters generated from reclustering, which could be categorized into three main subtypes (left) based on marker gene expression (right): $\gamma\delta$T_ITGAE (subcluster 0; *ITGAE*, *TRDV1*, *CLIC3*), $\gamma\delta$T_AREG (subcluster 1; *AREG*, *LTB*, *IL7R*) and $\gamma\delta$T_NKG7 (subcluster 2; *NKG7*, *LAG3*, *GNLY*). (**B**) Pie plot indicating the different ratios of each $\gamma\delta$T cell in GAS and UEA illustrating that $\gamma\delta$T_AREG and $\gamma\delta$T_NKG7 cells were only observed in GAS, and we classified $\gamma\delta$T_AREG and $\gamma\delta$T_NKG7 cells as "GAS-associated $\gamma\delta$T cells". (**C**) Predicted differentiation order of "GAS-associated $\gamma\delta$T cells" by CytoTRACE analysis. (**D**) Trajectory of differentiation of "GAS-associated $\gamma\delta$T cells" predicted by Monocle analysis. (**E**) Expression dynamics of selected marker genes, including stress-related genes (*XBP1*, *HSP90AB1*, and *BAG3*) and immune checkpoint genes (*CTLA4*, *LAG3*, and *TIGIT*). The color key from grey to red indicates relative expression levels from low to high. (**F**) Bar chart showing the enrichment of heat shock protein binding based on the GO pathways in "GAS-associated $\gamma\delta$T cells" presented with statistical significance [$-\mathrm{Log}_{10}$(*P* value)]. (**G**) Bar chart showing the enrichment of PD-L1 expression and PD-1 checkpoint pathway in cancer based on the pathway analysis in "GAS-associated $\gamma\delta$T cells" presented with statistical significance [$-\mathrm{Log}_{10}$(*P* value)]. (**H**) Bubble plot indicating the high expression level of genes associated with heat stress (*BAG3*, *HSPD1*, *HSPE1*, and *HSP90AB1*) in "GAS-associated $\gamma\delta$T cells". The colors represent the average expression levels and dot sizes represent the percentage expression of selected genes. (**I**) Bubble plot indicating the high expression level of genes associated with immune dysfunction (*LTB*, *LAG3*, *SERF2*, *PTPRCAP*, and *CD52*) in "GAS-associated $\gamma\delta$T cells". The colors represent the average expression levels and dot sizes represent the percentage expression of selected genes.

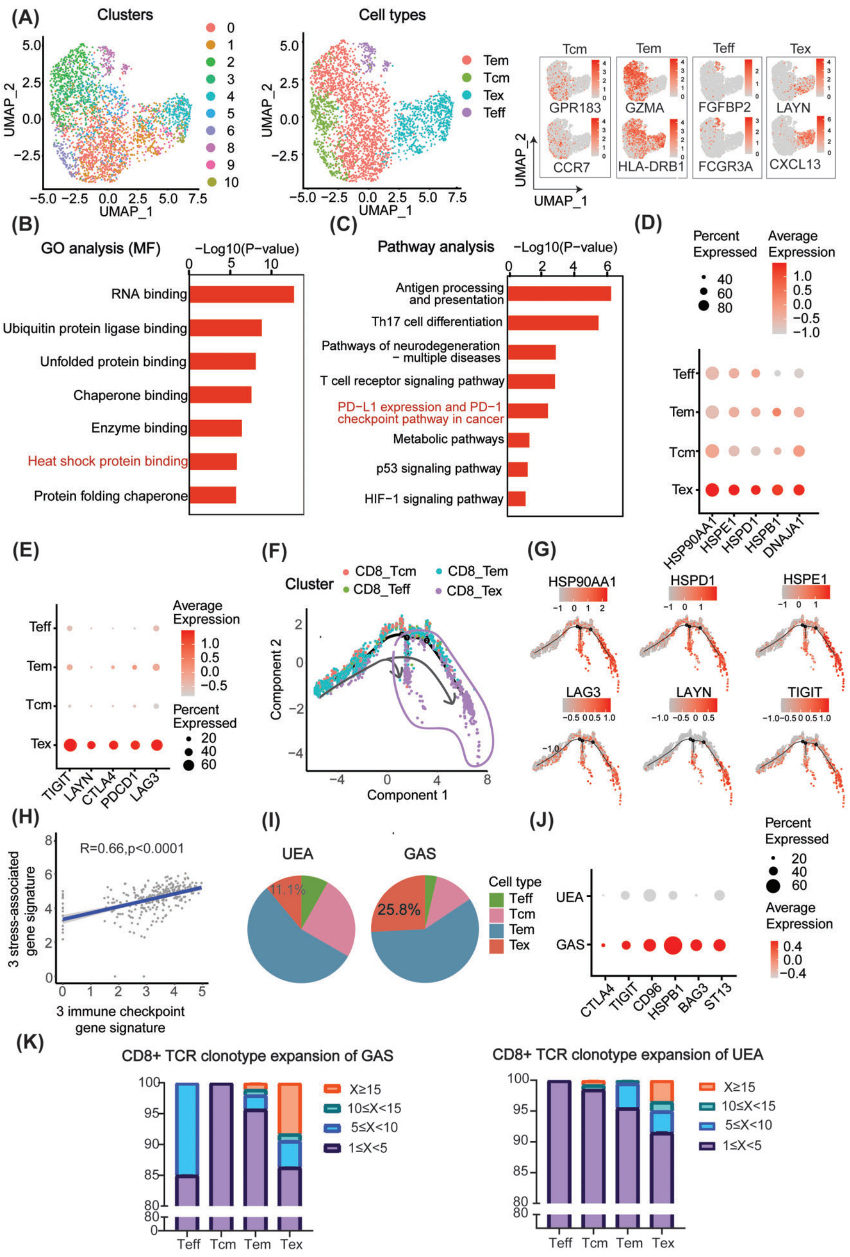

Figure 4 CD8+ Texs in GAS with accumulation of heat stress revealed immunosuppression. (**A**) UMAP plots of the 11 clusters generated from reclustering (left), which could be further categorized into 4 major groups (middle) according to marker gene expression (right): *GPR183* and *CCR7* for Tcms; *GZMA* and *HLA-DRB1* for Tems; *FGFBP2* and *FCGR3A* for Teffs; and *LAYN* and *CXCL13* for Texs. The color key from grey to red indicates relative expression levels from low to high. (**B**) Bar plot showing the enrichment of heat shock protein binding based on the GO pathways in Texs presented with statistical significance [$-\text{Log}_{10}(P\text{ value})$]. (**C**) Bar plot showing the enrichment of PD-L1 expression and PD-1 checkpoint pathway in cancer based on the pathway analysis in Texs presented with statistical significance [$-\text{Log}_{10}(P\text{ value})$]. (**D**) Bubble plots indicating the high expression level of genes associated with heat stress (*HSP90AA1*, *HSPE1*, *HSPD1*, *HSPB1*, and *DNAJA1*) in Texs. The colors represent the average expression levels and dot sizes represent the percentage expression of selected genes. (**E**) Bubble plots indicating the high expression level of genes associated with immune dysfunction (*TIGIT*, *LAYN*, *CTLA4*, *PDCD1*, and *LAG3*) in Texs. The colors represent the average expression levels and dot sizes represent the percentage expression of selected genes. (**F**) Differentiation trajectory of CD8+ T cell subclusters predicted by Monocle indicating the terminal location of Tex. (**G**) Predicted differentiation order of the expression of selected marker genes in CD8+ T cells including stress-related genes (*HSP90AA1*, *HSPD1*, and *HSPE1*) and immune checkpoint genes (*LAG3*, *LAYN*, and *TIGIT*). The color key from grey to red indicates relative expression levels from low to high. (**H**) Scatter plot indicating the positive association between three stress-associated gene signatures (*HSP90AA1*, *HSPD1*, and *HSPE1*) and three immune checkpoint-gene signatures (*LAG3*, *LAYN*, and *TIGIT*) (Pearson's correlation, $R = 0.66$). (**I**) Pie plots indicating the different ratios of each CD8+ T cell subtype in GAS and UEA, illustrating the significant abundance of Texs in GAS. (**J**) Bubble plot of stress-related genes (*HSPB1*, *BAG3*and *ST13*) and immune checkpoint genes (*CTLA4*, *TIGIT*and *CD96*) in GAS and UEA. The colors represent the average expression levels and dot sizes represent the percentage expression of selected genes. (**K**) Bar plot describing the TCR clonotype expansion of CD8+ T cells in GAS and UEA samples in four categories: $n = 1, 2 \le n < 5, 5 \le n < 15$, and $n > 15$. The results showed that CD8+ Texs in GAS harbored a higher degree of expanded clonotypes than those in UEA, implying greater immune exhaustion in GAS.

The crucial pathway and molecular events underlying GAS aggressiveness: CLU-associated heat shock pathway was a vital player in fostering stressful microenvironment and promoting immune escape in GAS

After reviewing the key cell subtypes playing significant roles in GAS aggressiveness (Fig. 5A), we were inspired to further investigate the crucial pathway underlying the malignant phenotype of GAS. To characterize the functional pathway of the key cell subtypes in GAS compared to UEA, we carried out gene set variation analysis (GSVA), through which we obtained the top 50 upregulated biological functional pathways of GAS epithelial cells, “GAS-enriched fibroblasts”, “GAS-associated $\gamma\delta$T cells”, and CD8+ Texs in GAS respectively, compared to epithelial cells, fibroblasts, $\gamma\delta$T cells, and CD8+ Texs in UEA. Inspiringly, we found that the heat shock protein pathway was one of the intersections of the upregulated functional pathways of GAS key cell subtypes closely corelated to the heat stress of GAS key cell subtypes stated above, including GAS epithelial cells, “GAS-enriched fibroblasts”, “GAS-associated $\gamma\delta$T cells”, and CD8+ Texs in GAS (Fig. 5B and supplementary Table 6, see online supplementary material), implying that heat shock pathway might play an indispensable role in fostering the unique stressful GAS TME.

Given the significant functional enrichment of the heat shock pathway in GAS epithelial cells and “GAS-enriched fibroblasts” which are known as the structural cells [39], the basic components of a tumor, we conducted DEG analysis of epithelial cells and fibroblasts, respectively, between GAS and UEA to further explore the pivotal molecular associated with the crucial heat shock pathway in the stressful GAS TME. Having acquired the top 50 highly expressed genes in GAS epithelial cells and “GAS-enriched fibroblasts” respectively, we took the intersection of these two sets and searched for the genes closely associated with the heat shock pathway (Fig. 5C and supplementary Table 7, see online supplementary material). Of note, *CLU*, which is reported to be closely associated with heat stress [40], was highly expressed in both GAS epithelial cells ($P < 0.05$) and “GAS-enriched fibroblasts” ($P < 0.001$) (Fig. 5D and supplementary Fig. 2, see online supplementary material). Besides, based on gene correlation analysis, we discovered that the expression level of *CLU* was positively correlated with that of other heat stress-related genes including *PDGFB*, *HSPA1B*, and *HSPB1* in GAS epithelial cells and “GAS-enriched fibroblasts” respectively (Fig. 5E and supplementary Fig. 3, see online supplementary material), among which the expression level of *PDGFB* showed the most significant correlation with that of *CLU* ($R = 0.47$, $P = 0.018$) (Fig. 5E). The results above not only indicated that GAS epithelial cells and “GAS-enriched fibroblasts” endured CLU-associated heat stress load but also highlighted that CLU might work as a crucial player in the heat shock pathway within the GAS microenvironment.

Having revealed not only GAS epithelial cells and “GAS-enriched fibroblasts” indicating CLU-associated heat stress, but also “GAS-associated $\gamma\delta$T cells” and CD8+ Texs in GAS manifesting immunosuppression with heat stress in GAS TME, we next investigated the unique cellular interactions among the above key cell subtypes in GAS (Fig. 5F). Notably, we discovered that (i) “GAS-enriched fibroblasts” highly expressing CLU had intercellular crosstalk with “GAS-associated $\gamma\delta$T cells” through the complement component 3 (*C3*)–complement component 3a receptor 1 (*C3AR1*) complex, which was associated with the dysfunction of T cells promoting tumor immune evasion; (ii) GAS epithelial cells characterized by high expression of CLU communicated with CD8+ Texs through the *CD155* (*PVR*)–*TIGIT* complex, indicating impaired antitumor immunity and immune escape. These findings suggest that the interactomes among GAS epithelial cells, “GAS-enriched fibroblasts”, and T cells (“GAS-associated $\gamma\delta$T cells” and CD8+ Texs) contribute to immunosuppression in the CLU-associated stressful GAS TME.

Taken together, the above results highlighted that CLU-associated heat shock pathway might act as a vital player in fostering the stressful GAS TME, in which cellular interactomes among the key cell types embodied CLU-associated heat stress load and immune escape, potentially facilitating GAS aggressiveness.

Clinical validation: CLU-associated stress contributes to immune escape and poor prognosis in GAS

Considering the potential crucial role of CLU-associated heat stress within GAS TME in aggravating the malignancy of GAS based on single-cell transcriptome analysis, we conducted in-depth clinical validation as follows. (i) Firstly, we conducted IHC staining on 25 GAS and 25 UEA samples to measure the differential expression level of CLU and PDGFB between GAS and UEA. The results showed that the expression of CLU and PDGFB is more remarkable in GAS tissues compared to UEA tissues ($P < 0.0001$), implying the presence of greater CLU-associated stress within GAS compared to UEA (Fig. 6A and supplementary Fig. 4A, see online supplementary material). (ii) In addition, through mIHC staining, we successfully confirmed not only the interaction of TIGIT–PVR between GAS epithelial cells (EPCAM+, CLU+) and CD8+ Texs (CD8+, LAYN+) (Fig. 6B) but also the interaction of C3–C3AR1 between “GAS-enriched fibroblasts” (COL1A1+, CLU+) and “GAS-associated $\gamma\delta$T cells” (TRGC1+, NKG7+) (Fig. 6C). Moreover, IHC staining exhibited significantly higher expression of C3 and TIGIT in GAS tissues compared to UEA tissues ($P < 0.01$) (Fig. 6D and supplementary Fig. 4B). These results indicate immune escape in the CLU-associated stressful GAS TME. (iii) Furthermore, to examine the correlation between CLU-associated stress and immune escape, we assessed the sensitivity and specificity of CLU expression in distinguishing high- from low-TIGIT groups and high- from low-C3 groups. ROC curve analysis was performed, and the area under the curve (AUC) values indicated that CLU expression effectively differentiated both group pairs ($AUC = 0.7384$; $AUC = 0.8264$) (Fig. 6E and F), supporting a significant positive correlation between CLU-associated stress and immune escape. (iv) We then constructed a four-gene signature comprising heat stress-related markers (*CLU*, *PDGFB*) and immunosuppression-related markers (*TIGIT*, *C3*). IHC staining confirmed significantly higher expression of all four genes in GAS compared to UEA ($P < 0.01$) (Fig. 6A and D). Based on TCGA CESC data, we discovered that the expression level of heat stress-related markers (*CLU*, *PDGFB*) was

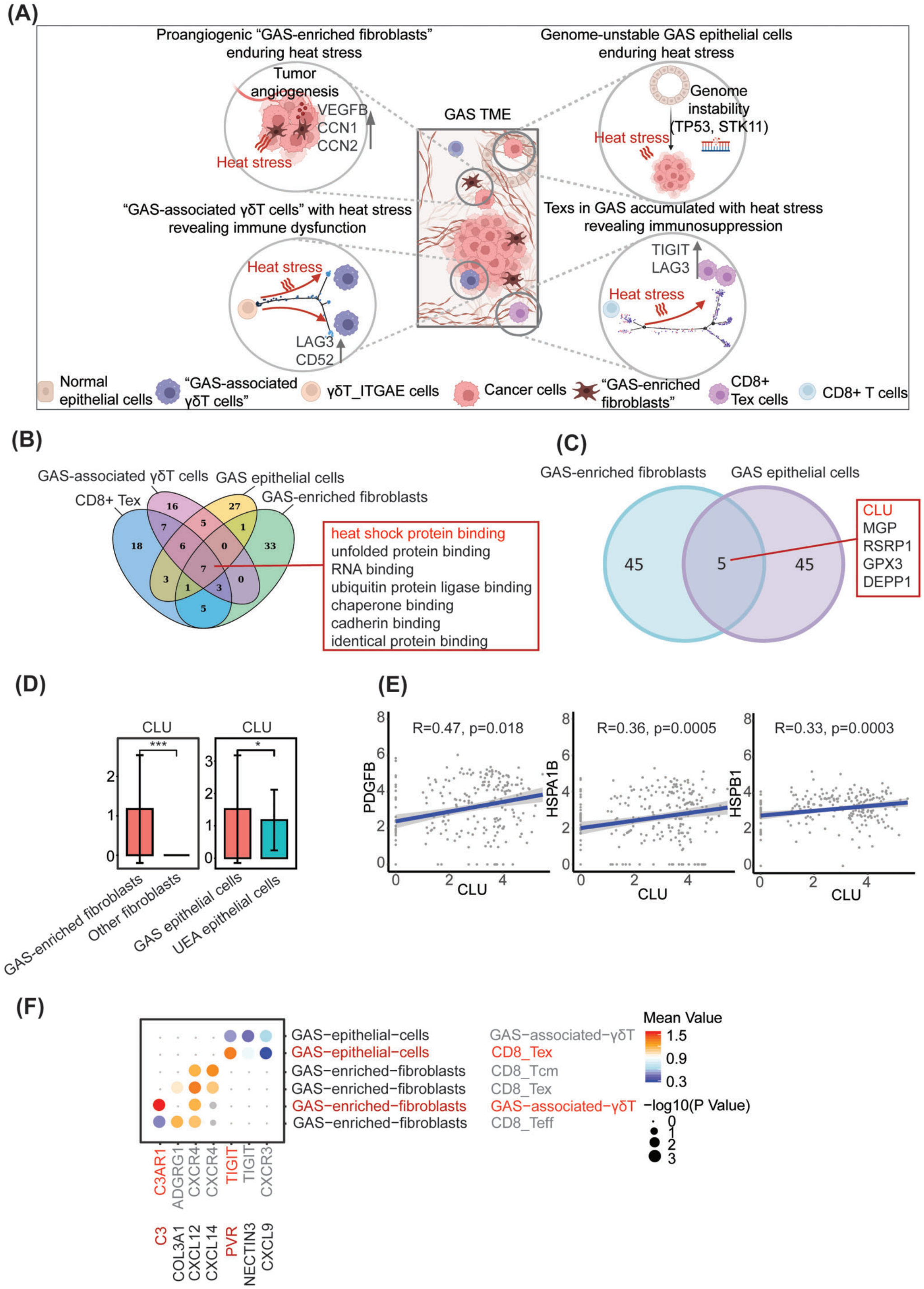

Figure 5 CLU-associated heat shock pathway was a crucial player in fostering a stressful microenvironment and promoting immunosuppression in GAS. (**A**) Schematic diagrams of features of key cell subtypes including GAS epithelial cells, "GAS-enriched fibroblasts", "GAS-associated $\gamma\delta$T cells", and CD8+ Texs in GAS in the GAS TME. Created in BioRender. Wu, T. (2026) https://BioRender.com/13rbplt. (**B**) Venn diagram showing the top 50 upregulated biological functional pathways of GAS epithelial cells, "GAS-enriched fibroblasts", "GAS-associated $\gamma\delta$T cells", and CD8+ Texs in GAS (*P* value < 0.05, fold-change > 1.5), compared to epithelial cells, fibroblasts, $\gamma\delta$T cells, and CD8+ Texs in UEA. (**C**) Venn diagram showing the top 50 upregulated genes of GAS epithelial cells and "GAS-enriched fibroblasts" (*P* value < 0.05, fold-change > 1.5), compared to epithelial cells and fibroblasts in UEA. (**D**) Box plot indicating the higher expression level of *CLU* in "GAS-enriched fibroblasts" and GAS epithelial cells, compared to other fibroblasts and UEA epithelial cells. *P* values were obtained by Student's t-test. $^{*}P < 0.05$; $^{***}P < 0.001$. (**E**) Scatter plot indicating the positive association between *CLU* and other stress-related genes, including *CLU* and *PDGFB* (Pearson's correlation, $R = 0.47$), *CLU* and *HSPA1B* (Pearson's correlation, $R = 0.36$), and *CLU* and *HSPB1* (Pearson's correlation, $R = 0.33$). (**F**) Dot plots demonstrate selected ligand–receptor interactions among key cell subtypes in GAS TME including GAS epithelial cells, "GAS-enriched fibroblasts", "GAS-associated $\gamma\delta$T cells", and CD8+ Texs in GAS. The involved cell types and ligand–receptor interactions are indicated by columns and rows, respectively. The means of the average expression levels of two interacting molecules are indicated by the color key, with blue to red representing low to high expression, respectively. The [-Log$_{10}$(*P* values)] are indicated by dot size.

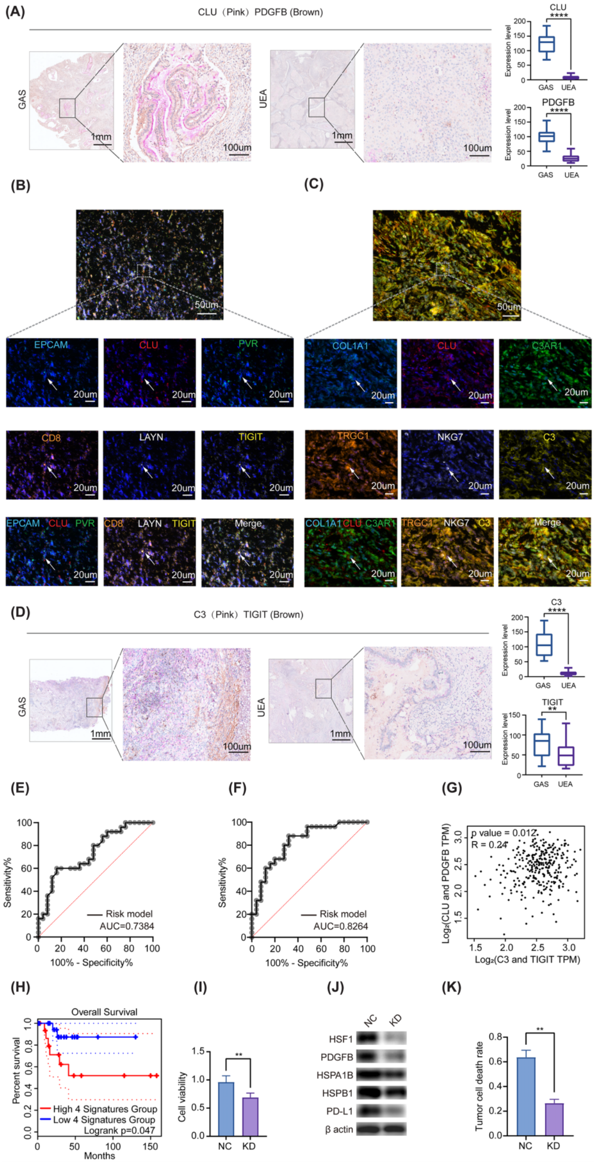

Figure 6 Validation of CLU-associated heat stress and its potential role in promoting immunosuppression in GAS TME. (**A**) Representative immunohistochemistry images of a clinical specimen showing the expression levels of CLU and PDGFB in GAS and UEA. Original magnification: ×2.5, scale bar: 1mm (left); ×200, scale bar:100 μm (right). Data are presented as the mean ± SEM. *P* values were calculated using the Student's t-test. $^{****}P < 0.0001$. Expression level was calculated by dividing the IOD value by the area of the target cells. (**B**) Representative images of mIHC staining of the interaction of TIGIT-PVR between GAS epithelial cells (EPCAM+, CLU+) and CD8+ Texs (CD8+, LAYN+). Proteins that were detected using the respective antibodies are indicated on the top. The cyan, red, green, orange, white, and yellow arrows indicate cells in GAS tissue samples with positive expression of the EPCAM, CLU, PVR, CD8, LAYN, and TIGIT proteins, respectively (bottom panel). Scale bars, 50 μm and 20 μm for the top and bottom panels, respectively. (**C**) Representative images of mIHC staining of the interaction of C3-C3AR1 between "GAS-enriched fibroblasts" (COL1A1+, CLU+) and "GAS-associated $\gamma\delta$T cells" (TRGC1+, NKG7+). Proteins that were detected using the respective antibodies are indicated on the top. The cyan, red, green, orange, white, and yellow arrows indicate cells in GAS tissue samples with positive expression of the COL1A1, CLU, C3AR1, TRGC1, NKG7, and C3 proteins, respectively (bottom panel). Scale bars, 50 μm and 20 μm for the top and bottom panels, respectively. (**D**) Representative immunohistochemistry images of a clinical specimen showing the expression levels of C3 and TIGIT in GAS and UEA. Original magnifications: ×2.5, scale bar: 1mm (left); ×200, scale bar: 100 μm (right). Data are presented as the mean ± SEM. *P* values were calculated using the student's t test. $^{**}P < 0.01$; $^{****}P < 0.0001$. (**E**) ROC curve analysis of the variations of CLU expression level in high-TIGIT group and low-TIGIT group. (**F**) ROC curve analysis of the variations of CLU expression level in high-C3 group and low-C3 group. (**G**) Scatter plot indicating the positive association between heat stress makers (*CLU* and *PDGFB*) and immunosuppressive makers (*C3* and *TIGIT*) (Pearson's correlation, $R = 0.24$) (**H**) Kaplan–Meier curves of the four-gene signature low expression group (lower 25%, $n = 24$) and the four-gene signature high expression group (higher 25%, $n = 24$) with significant statistical difference based on TCGA CESC database demonstrating a poorer OS of the four-gene signature high expression group. (**I**) HT-3-*CLU* KD cells showed reduced proliferation compared to their respective controls ($n = 5$ per group). *P* values were calculated using the Student's t-test. $^{**}P < 0.01$. (**J**) Western blot results demonstrated the expression of HSF1, PDGFB, HSPA1B, HSPB1, and PD-L1 protein in HT-3-NC and HT-3-*CLU* KD cells, with downregulation in HT-3-*CLU* KD compared to their respective controls; $n = 5$ per group. (**K**) Cisplatin (DDP) significantly reduced tumor cell mortality rates in HT-3-*CLU* KD compared to their respective controls. ($n = 5$ per group). *P* values were calculated using the Student's t-test. $^{**}P < 0.01$.

positively correlated with immunosuppression-related markers (*TIGIT*, *C3*) in CC ($R = 0.24$; $P < 0.05$) (Fig. 6G). Moreover, based on TCGA CESC data, patients with higher expression of this four-gene signature showed reduced overall survival ($P < 0.05$) (Fig. 6H), suggesting that CLU-associated stress and immune dysfunction collectively contribute to poor prognosis in CC patients.

In summary, we verified the presence of a CLU-associated stressful TME in GAS via IHC and mIHC staining and established a positive link between CLU-related stress and immune escape. A corresponding four-gene signature (*CLU*, *PDGFB*, *TIGIT*, and *C3*) representing poor prognosis in CC patients was developed, which correlated with poorer survival in GAS patients. These clinical findings underscore the critical role of CLU-associated stressful TME in GAS aggressiveness and offer insights for CLU-targeted therapeutic strategies.

Functional validation: CLU plays a multifaceted role in heat stress and immune escape

To systematically investigate CLU's dual role in forming CLU-associated stressful TME and promoting immune escape, we established HT-3 *CLU* knockdown (KD) as experimental models, with transfection efficiency validated by quantitative real-time PCR and western blotting (supplementary Fig. 5A and B, see online supplementary material). Of note, (i) *CLU* KD markedly suppressed proliferative capacity ($P < 0.01$) (Fig. 6I). (ii) Intriguingly, *CLU* KD significantly reduced the expression level of heat shock transcription factor 1 (HSF1), the master transcriptional regulator of the heat shock response [41], along with downregulation of heat stress associated proteins (PDGFB, HSPA1B, and HSPB1), suggesting that CLU exerts a feed-forward regulation on HSF1, thereby attenuating the heat stress response of the KD group compared with the negative control (NC) group (Fig. 6J). (iii) Furthermore, *CLU* KD lowered programmed death-ligand 1 (PD-L1) expression in HT-3 cells, implying a potential role of CLU in promoting immune escape (Fig. 6J). (iv) Importantly, treatment with cisplatin (DDP) resulted in more tumor cell death in the HT-3-*CLU* KD group compared with NC group ($P < 0.01$) (Fig. 6K). To summarize, the above findings position CLU as an attractive therapeutic target in GAS, offering the potential to arrest CLU-associated stress and immunosuppression, and sensitize chemotherapy.

Therapeutic insights: OGX-011 targeting CLU might serve as a promising therapeutic strategy for GAS based on 3D GAS-derived tumoroids

GAS-derived tumoroids: miniature replicas of the key features, especially CLU-associated stress of original tumor tissue, were established

Given the absence of cell lines that recapitulate the core features of GAS, well-established experimental models are currently lacking. Therefore, we innovatively constructed GAS-derived tumoroids and utilized them as a platform to model GAS tumor characteristics *in vitro* (Fig. 7A). (i) IHC staining demonstrated that positive expression of PAX8, HIK1083, MUC6, and TFF2, which are known indicators of GAS biomarkers [42, 43], were observed in the GAS tumoroids (Fig. 7B). (ii) In addition, GAS-derived tumoroids had positive expression of CLU, implying CLU-associated stress in GAS-derived tumoroids in accordance with the TME of the original tissues (Fig. 7C). (iii) Importantly, WGS analysis demonstrated a highly consistent mutation landscape between primary tumor tissue and GAS-derived tumoroids (Fig. 7D and E). We also observed the presence of frequently mutated genes (*TP53*, *KRAS*, *STK11*), further confirming the stable maintenance of the core mutation profile in GAS (Fig. 7D). Overall, our findings revealed that the established GAS-derived tumoroids recapitulated the histologic features, CLU-associated stressful properties, and genetic characteristics of the parental tumor.

Clinical insights based on GAS-derived tumoroids: OGX-011 targeting CLU could serve as an effective precise treatment for GAS

Owing to the crucial role of CLU within GAS TME, we hypothesized that targeting CLU could serve as an effective precise therapy for GAS patients. Therefore, we conducted *in vitro* validation using the GAS-derived tumoroid models to evaluate the tumor suppression potential of OGX-011, a CLU inhibitor, alone and combined with DDP. Encouragingly, the results demonstrated that OGX-011 not only inhibited GAS tumoroid growth but also sensitized GAS tumoroid to DDP treatment. To be more specific, OGX-011 combined with DDP treatment exhibited greater anti-tumor effect than either OGX-011 or DDP alone *in vitro* ($P < 0.05$) (Fig. 7F), illustrating the potential clinical benefit from using OGX-011 combined with DDP treatment for GAS patients. Besides, western blotting and IHC staining of GAS-derived tumoroids showed that OGX-011 treatment resulted in a more apparent reduction of CLU and PDGFB comparable to DDP monotherapy (Fig. 7G and H), demonstrating that CLU inhibition reduces heat stress in GAS tumoroid. These findings validated that targeting CLU suppressed tumor growth, decreased cellular stress, and increased the efficacy of DDP therapy, providing critical clues for the development of more effective therapy for GAS.

Discussion

GAS, as the most common subtype of NHPVA ADC with aggressive biological behavior and poor prognosis, still remains a treatment-refractory disease [35]. A limited understanding of the clinical features and pathogenesis of GAS poses a huge challenge for the accurate diagnosis and precise treatment of GAS. To address such dilemmas, we conducted a comprehensive investigation into the clinicopathological features, key cell subtypes in the TME, crucial pathways and molecular events, as well as a targeted therapeutic approach to GAS.

GAS is a clinically aggressive cervical cancer with distinctive histopathologic features [5, 10]. In the present study, our clinical data revealed that NHPVA ADC, of which GAS accounted for the highest proportion, showed more widespread involvement, higher misdiagnosis rate, and poorer prognosis compared to HPVA ADC. However, these findings should be interpreted with caution due to the limited sample size of our clinical cohort. Prior studies have also highlighted the distinct clinicopathological features of GAS, including its tendency for deep stromal invasion, frequent misdiagnosis as HPVA ADC, and an overall unfavorable

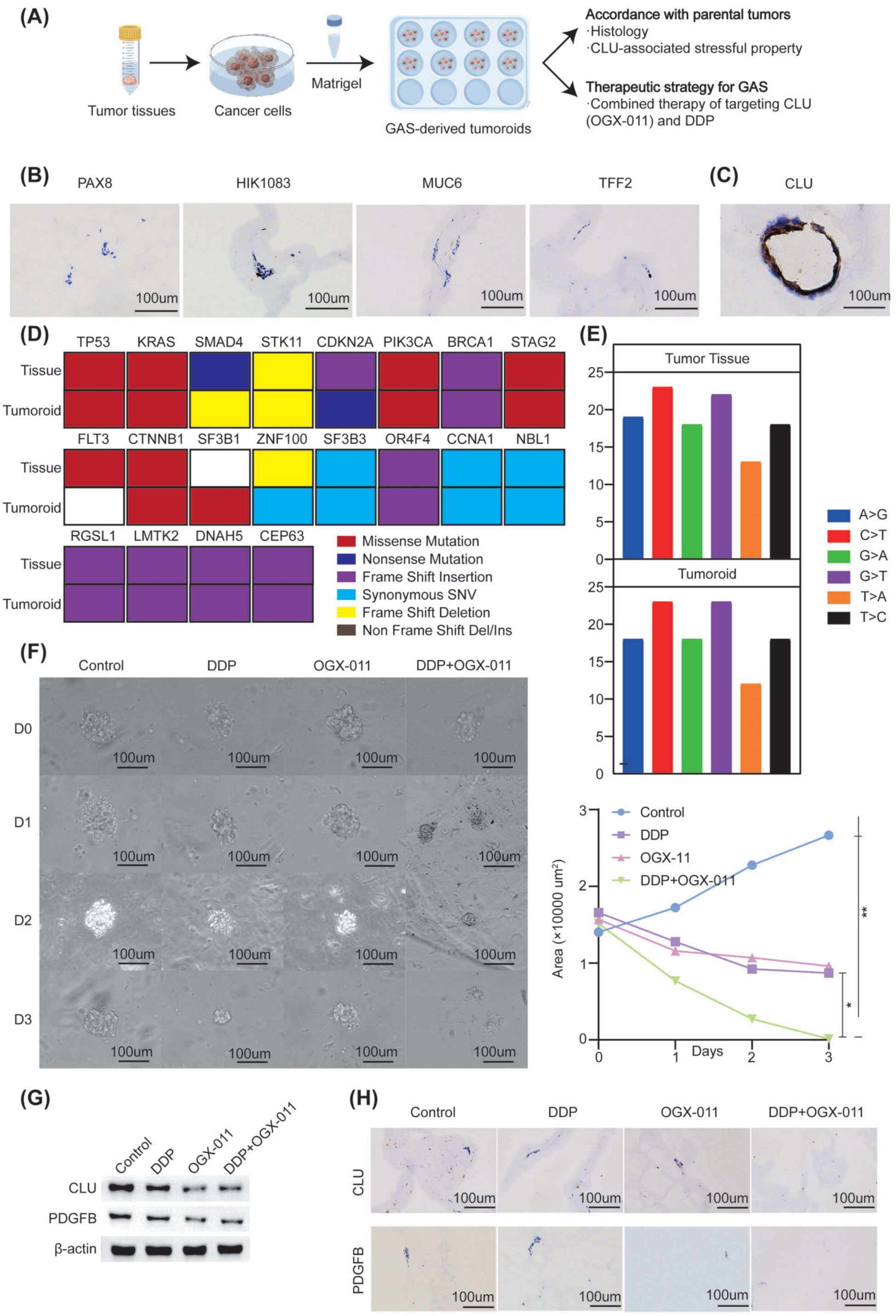

Figure 7 Construction of 3D GAS-derived tumoroids and *in vitro* validation of OGX-011 targeting CLU as promising therapy to relieve heat stress, inhibit tumor growth, and sensitize DDP. (**A**) Schematic diagram of building 3D GAS-derived tumoroids and *in vitro* experiments. (**B**) Representative IHC images of 3D GAS-derived tumoroids including PAX8+ tumoroids, HIK1083+ tumoroids, MUC6+ tumoroids, and TFF2+ tumoroids. Original magnifications: ×200. Scale bar: 100 μm. (**C**) Representative IHC images of CLU + 3D GAS-derived tumoroids. Original magnification: ×200. Scale bar: 100 μm. (**D**) Heatmap showing the top 20 gene mutation type in GAS-derived tumoroid and original tumor tissue. (**E**) Bar graphs displaying the different contributions of SNV in GAS-derived tumoroid and original tumor tissue. (**F**) Representative bright field images of 3D GAS-derived tumoroids in control group, DDP treatment group, anti-CLU (OGX-011) treatment group, and combined treatment group (DDP + OGX-011). Original magnifications: ×200. Scale bar: 100 μm. Quantification of GAS-derived tumoroids area are shown on the right. Data are presented as the mean ± SEM. *P* values were obtained by one-way ANOVA with Tukey's $^{*}P < 0.05$; $^{**}P < 0.01$. (**G**) Western blot results demonstrate the expression of CLU protein and PDGFB protein in control group, DDP treatment group, anti-CLU (OGX-011) treatment group and combined treatment group (DDP + OGX-011), with downregulation of CLU and PDGFB protein in anti-CLU (OGX-011) treatment group and combined treatment group (DDP + OGX-011) ($n = 3$ per group). (**H**) Representative IHC images of 3D GAS-derived tumoroids including CLU + tumoroids and PDGFB + tumoroids in control group, DDP treatment group, anti-CLU (OGX-011) treatment group, and combined treatment group (DDP + OGX-011). Original magnifications: ×200. Scale bar: 100 μm.

clinical outcome [44–47], further supporting the observations reported here. With regard to the pathogenic mechanisms behind such aggressive phenotype of GAS, researchers have already identified some genomic drivers [44, 48]. However, to our knowledge, there are few in-depth studies investigating the oncogenic mechanism underlying the malignant clinical phenotype of GAS from the perspective of TME, which greatly affects disease initiation and progression [49]. Therefore, we integrated scRNA-seq with TCR-seq to systematically explore the core features of TME in GAS. (i) Regarding key cell subtypes in GAS TME, we discovered that genome-unstable GAS epithelial cells, proangiogenic "GAS-enriched fibroblasts" and T cells revealing immunosuppression in GAS ("GAS-associated $\gamma\delta$T cells" and CD8 + Texs in GAS) endured great heat stress and contributed to the aggressive phenotype of GAS. (ii) Regarding the crucial pathways and molecular events contributing to the unique stressful GAS TME, we innovatively demonstrated that the CLU-associated heat shock pathway played an important role in fostering the unique heat stress within GAS TME. CLU is known to protect tumor cells under stress conditions, such as conventional therapies [50–54]. Consistently, we found that *CLU* knockdown suppresses HSF1 expression, implicating CLU in regulating the HSF1-mediated heat shock response [55, 56]. Thus, we propose a feed-forward loop wherein CLU potentiates HSF1 expression and, consequently, increases the levels of heat stress-associated proteins (e.g. PDGFB, HSPA1B, HSPB1), thereby enhancing heat stress and facilitating GAS tumor progression. (iii) Regarding immunosuppression underlying CLU-associated heat stress in GAS, we observed related cellular interactomes, such as C3–C3AR1 interaction between "GAS-enriched fibroblasts" highly expressing CLU and "GAS-associated $\gamma\delta$T cells" as well as PVR–TIGIT interaction between GAS epithelial cells highly expressing CLU and CD8+ Texs, indicating immune dysfunction potentially related to CLU-associated stress within GAS TME. Furthermore, we found that *CLU* knockdown reduced PD-L1 expression in CC cells, suggesting the potent role of CLU in promoting immune escape. This aligns with reports linking high CLU expression to diminished immune response [57, 58]. Notably, although CLU-induced immunosuppression has been associated with STAT3 activation [59], the specific mechanism by which CLU facilitates immune escape within the GAS TME remains unclear and warrants further investigation. (iv) Regarding clinical validation, we confirmed the CLU-associated stressful TME within GAS by IHC staining and validated cellular interactomes representing immune escape in the CLU-associated stressful microenvironment of GAS through mIHC staining. Importantly, analysis of TCGA data confirmed a close link between CLU-associated stress and immune escape in CC, leading to a prognostic four-gene signature encompassing heat stress (*CLU*, *PDGFB*) and immunosuppression (*TIGIT*, *C3*) markers. However, this association and the prognostic value of the signature remain to be validated specifically in GAS and across larger cohorts. All in all, we innovatively unveiled the key cell subtypes associated with heat stress contributing to the malignant phenotype of GAS, and proposed CLU playing a vital role in fostering the unique stressful TME and immune escape collectively contributing to poor clinical outcomes of GAS, providing novel insights into the unique malignant microenvironment of GAS, and offering potential clues for CLU-targeted therapy in GAS.

It is reported that the response rate of GAS patients to standard chemotherapy, DDP, remains poor [60, 61]. Given that CLU plays a significant role in modulating the sensitivity of DDP by the phosphorylated extracellular signal-regulated kinase 1/2 (pERK1/2) and phosphorylated AKT (pAKT) pathways in other cancers [62–64], and our results showed that GAS TME was characterized by CLU-associated stress making a great contribution to the malignant phenotype and poor prognosis of GAS, we wondered whether CLU could serve as a potential therapeutic target and improve the efficacy of DDP for GAS patients. To answer such a question, effective models for GAS are urgently needed. We first validated that *CLU* knockdown alleviates heat stress and immune escape and sensitizes cells to DDP using the HT-3 cell line. However, as an HPV-negative cervical cancer line, HT-3 differs in cellular origin from GAS [65]. Given the current lack of a recognized GAS cell line, we established GAS-derived tumoroids for the first time and confirmed the biomimic properties of the tumoroids, revealing consistency of histological features, the unique CLU-mediated stressful microenvironment, and the genetic characteristics of the original tissues, providing a powerful model to support subsequent preclinical exploration of GAS precision therapy. Based on the construction of 3D GAS-derived tumoroids, we further assessed the efficacy of CLU inhibitor, OGX-011, alone and combined with DDP for GAS. Our data demonstrate that OGX-011 monotherapy reduces heat stress and tumor growth. Furthermore, its combination with DDP showed superior efficacy compared to either agent alone, indicating that CLU-targeting enhances chemosensitivity. Notably, the translational potential of this approach is supported by the prior evaluation of OGX-011 in phase II clinical trials for other cancers (e.g. prostate and breast) [66, 67]. Consequently, our findings bolster confidence in pursuing OGX-011 as a promising therapeutic candidate for GAS. To further validate CLU as a target, future studies employing CRISPR-mediated gene editing in GAS tumoroids would provide more definitive mechanistic proof. In summary, by innovatively establishing a 3D GAS tumoroid model, we have validated that CLU-targeted therapy with OGX-011 alleviates heat stress, inhibits tumor growth, and sensitizes GAS to chemotherapy.

Several limitations should be considered. First, the clinical cohort for single-cell analysis was limited by the rarity of GAS and the stringent requirements for sequencing, potentially affecting the assessment of tumor heterogeneity and the generalizability of these preliminary findings. We plan to address this by sequencing additional samples in the future. It is also important to note that, in the absence of an established GAS cell line, CLU functionality was verified using the HT-3 line, a NHPVA CC cell line, which is a recognized methodological constraint. Besides, the therapeutic validation of OGX-011 was confined to *in vitro* tumoroid models. The translational relevance would be strengthened by future *in vivo* studies using patient-derived xenograft or patient-derived xenograft organoid models. Furthermore, the detailed mechanisms by which CLU regulates HSF1 and PD-L1 within the GAS TME warrant further investigation.

In conclusion, (i) we firstly confirmed more aggressive clinicopathological characteristics and poorer prognosis of GAS compared with UEA, through clinical data from our center. (ii) To explore the pathogenic mechanisms behind the aggressive phenotype of GAS, we unraveled the core features of GAS using scRNA-seq and TCR-seq. Notably, key cell subtypes including GAS epithelial cells, "GAS-enriched fibroblasts," and T cells ("GAS-associated $\gamma\delta$T cells" and CD8+ Texs in GAS) in GAS TME endured heat stress and potentially contributed to the formation of the aggressive phenotype of GAS. More importantly, we innovatively deciphered the CLU-associated heat stress of key cell subtypes in GAS that play a vital role in fostering the stressful GAS TME. Furthermore, we observed that cellular interactomes among the key cell subtypes of GAS, embodying CLU-associated stress and immune escape, contributed to the malignancy of GAS. (iii) Through validation, we suggested the potent role of CLU in fostering heat stress and immune escape, highlighted the significant association between CLU-associated stress and immune escape based on the TCGA database, and thereby established a four-gene signature (*CLU*, *PDGFB*, *TIGIT*, and *C3*), indicating correlation between poor prognosis and CLU-associated stress and immune escape in GAS. (iv) Furthermore, we pioneeringly established 3D GAS-derived tumoroids, replicating the morphological features, the unique CLU-associated stressful microenvironment, and genetic profile of the original tissue, which can be used as a reliable research model for GAS. (v) Importantly, based on the *in vitro* 3D GAS-derived tumoroid model, we validated the anti-tumor effect as well as the sensitizing DDP efficacy of OGX-011 by targeting CLU. All in all, our investigation not only demonstrated that CLU-associated heat stress of key cell subtypes (GAS epithelial cells, "GAS-enriched fibroblasts", "GAS-associated $\gamma\delta$T cells", and CD8+ Texs in GAS) is crucial in fostering the unique stressful and immunosuppressive GAS microenvironment, but also innovatively constructed 3D GAS-derived tumoroids and validated the feasibility of CLU-targeted therapy (OGX-011) as a promising treatment strategy for GAS, providing significant clinical value.

Ethics statement

The current study was approved by the Ethics Committee of Obstetrics and Gynaecology Hospital of Fudan University (No. 2022-105), and complied with the declaration of Helsinki. Informed consent was obtained from all participants.

Acknowledgments

This project was supported by funding from Medical Innovation Research of Shanghai Science and Technology (grant No. 22Y31900500 to K.H. and grant No.21Y11906900 to J.Q.), National Natural Science Foundation of China (grant No. 82173188 to K.H. and grant No. 82472993 to J.Q.), Shanghai Municipal Hospital Development Center (grant No. SHDC22021307 to K.H.), and Shanghai Municipal Health Commission (grant No. 202040498 to J.Q.).

Author contributions

Tong Wu (Conceptualization, Data curation, Visualization, Writing—original draft), Xinyu Qu (Visualization, Writing—review & editing), Lili Jiang (Conceptualization, Methodology), Tingting Ren (Validation), Qinqin Liu (Resources, Software), Xingyu Chang (Resources, Supervision), Meng Xie (Resources, Writing—review & editing), Keqin Hua (Funding acquisition, Writing—review & editing), and Junjun Qiu (Funding acquisition, Writing— review & editing).

Supplementary material

Supplementary material is available at *PCMEDI Journal* online.

References

1. Sung H, Ferlay J, Siegel RL *et al.* Global cancer statistics 2020: GLOBOCAN estimates of incidence and mortality worldwide for 36 cancers in 185 countries. *CA Cancer J Clin* 2021;**71**:209–49. https://doi.org/10.3322/caac.21660
2. Stolnicu S, Barsan I, Hoang L *et al.* International Endocervical Adenocarcinoma Criteria and Classification (IECC): A New Pathogenetic Classification for Invasive Adenocarcinomas of the Endocervix. *Am J Surg Pathol* 2018;**42**:214–26. https://doi.org/10.1097/PAS.0000000000000986
3. Hodgson A, Olkhov-Mitsel E, Howitt BE *et al.* International Endocervical Adenocarcinoma Criteria and Classification (IECC): correlation with adverse clinicopathological features and patient outcome. *J Clin Pathol* 2019;**72**:347–53. https://doi.org/10.1136/jclinpath-2018-205632
4. Lyu BJ, Shi HY, Shao Y *et al.* Endocervical adenocarcinomas classified by International Endocervical Adenocarcinoma Criteria and Classification: a clinicopathological and prognostic analysis of 286 cases. *Chinese Journal of Pathology* 2021;**50**:1014–9.
5. Kusanagi Y, Kojima A, Mikami Y *et al.* Absence of high-risk human papillomavirus (HPV) detection in endocervical adenocarcinoma with gastric morphology and phenotype. *Am J Pathol* 2010;**177**:2169–75. https://doi.org/10.2353/ajpath.2010.100323
6. Li GL, Jiang W, Gui SQ *et al.* Minimal deviation adenocarcinoma of the uterine cervix. *Intl J Gynecology & Obste* 2010;**110**:89–92. https://doi.org/10.1016/j.ijgo.2010.03.016
7. Kido A, Mikami Y, Koyama T *et al.* Magnetic resonance appearance of gastric-type adenocarcinoma of the uterine cervix in comparison with that of usual-type endocervical adenocarcinoma a pitfall of newly described unusual subtype of endocervical adenocarcinoma. *Int J Gynecol Cancer* 2014;**24**:1474–9. https://doi.org/10.1097/IGC.0000000000000229
8. Talia KL, McCluggage WG. The developing spectrum of gastric-type cervical glandular lesions. *Pathology (Phila)* 2018;**50**:122–33. https://doi.org/10.1016/j.pathol.2017.09.009
9. Kojima A, Shimada M, Mikami Y *et al.* Chemoresistance of gastric-type mucinous carcinoma of the uterine cervix: a study of the sankai gynecology study group. *Int J Gynecol Cancer* 2018;**28**:99–106. https://doi.org/10.1097/igc.0000000000001145
10. Nishio S, Mikami Y, Tokunaga H *et al.* Analysis of gastric-type mucinous carcinoma of the uterine cervix—An aggressive tumor with a poor prognosis: A multi-institutional study. *Gynecol Oncol* 2019;**153**:13–9. https://doi.org/10.1016/j.ygyno.2019.01.022
11. Nishio S, Matsuo K, Nasu H *et al.* Analysis of postoperative adjuvant therapy in 102 patients with gastric-type mucinous carcinoma of the uterine cervix: A multiinstitutional study. *Eur J Surg Oncol* 2022;**48**:2039–44. https://doi.org/10.1016/j.ejso.2022.03.007
12. Karamurzin YS, Kiyokawa T, Parkash V *et al.* Gastric-type endocervical adenocarcinoma an aggressive tumor with unusual metastatic patterns and poor prognosis. *Am J Surg Pathol* 2015;**39**:1449–57. https://doi.org/10.1097/PAS.0000000000000532

13. Lu SS, Shi JP, Zhang XB *et al.* Comprehensive genomic profiling and prognostic analysis of cervical gastric-type mucinous adenocarcinoma. *Virchows Arch* 2021;**479**:893–903. https://doi.org/10.1007/s00428-021-03080-y
14. Selenica P, Alemar B, Matrai C *et al.* Massively parallel sequencing analysis of 68 gastric-type cervical adenocarcinomas reveals mutations in cell cycle-related genes and potentially targetable mutations. *Mod Pathol* 2021;**34**:1213–25. https://doi.org/10.1038/s41379-020-00726-1
15. Hinshaw DC, Shevde LA. The Tumor Microenvironment Innately Modulates Cancer Progression. *Cancer Res* 2019;**79**:4557–66. https://doi.org/10.1158/0008-5472.CAN-18-3962
16. Maacha S, Bhat AA, Jimenez L *et al.* Extracellular vesicles-mediated intercellular communication: roles in the tumor microenvironment and anti-cancer drug resistance. *Mol Cancer* 2019;**18**:1–55. https://doi.org/10.1186/s12943-019-0965-7
17. Sklavenitis-Pistofidis R, Getz G, Ghobrial I. Single-cell RNA sequencing: one steP closer to the clinic. *Nat Med* 2021;**27**:375–6. https://doi.org/10.1038/s41591-021-01276-y
18. Afzal S, Gil-Farina I, Gabriel R *et al.* Systematic comparative study of computational methods for T-cell receptor sequencing data analysis. *Briefings Bioinf* 2019;**20**:222–34. https://doi.org/10.1093/bib/bbx111
19. Heather JM, Ismail M, Oakes T *et al.* High-throughput sequencing of the T-cell receptor repertoire: pitfalls and opportunities. *Briefings Bioinf* 2018;**19**:554–65.
20. Simian M, Bissell MJ. Organoids: A historical perspective of thinking in three dimensions. *J Cell Biol* 2017;**216**:31–40. https://doi.org/10.1083/jcb.201610056
21. Krishna C, DiNatale RG, Kuo F *et al.* Single-cell sequencing links multiregional immune landscapes and tissue-resident T cells in ccRCC to tumor topology and therapy efficacy. *Cancer Cell* 2021;**39**:662–77. https://doi.org/10.1016/j.ccell.2021.03.007
22. Losic B, Craig AJ, Villacorta-Martin C *et al.* Intratumoral heterogeneity and clonal evolution in liver cancer. *Nat Commun* 2020;**11**:1–291.https://doi.org/10.1038/s41467-019-14050-z
23. Hui ZZ, Zhang JL, Ren YL *et al.* Single-cell profiling of immune cells after neoadjuvant pembrolizumab and chemotherapy in IIIA non-small cell lung cancer (NSCLC). *Cell Death Dis* 2022;**13**:607. https://doi.org/10.1038/s41419-022-05057-4
24. Ashburner M, Ball CA, Blake JA *et al.* Gene Ontology: tool for the unification of biology. *Nat Genet* 2000;**25**:25–9. https://doi.org/10.1038/75556
25. Draghici S, Khatri P, Tarca AL *et al.* A systems biology approach for pathway level analysis. *Genome Res* 2007;**17**:1537–45. https://doi.org/10.1101/gr.6202607
26. Gulati GS, Sikandar SS, Wesche DJ *et al.* Single-cell transcriptional diversity is a hallmark of developmental potential. *Science* 2020;**367**:405–11. https://doi.org/10.1126/science.aax0249
27. Vento-Tormo R, Efremova M, Botting RA *et al.* Single-cell reconstruction of the early maternal-fetal interface in humans. *Nature* 2018;**563**:347–53. https://doi.org/10.1038/s41586-018-0698-6
28. Yaari G, Bolen CR, Thakar J *et al.* Quantitative set analysis for gene expression: a method to quantify gene set differential expression including gene-gene correlations. *Nucleic Acids Res* 2013;**41**:e170. https://doi.org/10.1093/nar/gkt660
29. Lonconanco E, Navarrete F, Cuevas N *et al.* Integrated optical density analysis of the immunohistochemical expression of the progesterone receptor in the uterine endometrium of prepubertal araucana sheep. *Int J Morphol* 2021;**39**:1278–82. https://doi.org/10.4067/S0717-95022021000501278
30. Mansour AA, Gonçalves JT, Bloyd CW *et al.* An *in vivo* model of functional and vascularized human brain organoids. *Nat Biotechnol* 2018;**36**:432–41. https://doi.org/10.1038/nbt.4127
31. Raczy C, Petrovski R, Saunders CT *et al.* Isaac: ultra-fast whole-genome secondary analysis on Illumina sequencing platforms. *Bioinformatics* 2013;**29**:2041–3. https://doi.org/10.1093/bioinformatics/btt314
32. Chen XY, Schulz-Trieglaff O, Shaw R *et al.* Manta: rapid detection of structural variants and indels for germline and cancer sequencing applications. *Bioinformatics* 2016;**32**:1220–2. https://doi.org/10.1093/bioinformatics/btv710
33. Kim S, Scheffler K, Halpern AL *et al.* Strelka2: fast and accurate calling of germline and somatic variants. *Nat Methods* 2018;**15**:591–4. https://doi.org/10.1038/s41592-018-0051-x
34. Birchmeier W, Birchmeier C. Epithelial-mesenchymal transitions in development and tumor progression. *EXS* 1995;**74**:1–15.
35. Park E, Kim SW, Kim S *et al.* Genetic characteristics of gastric-type mucinous carcinoma of the uterine cervix. *Mod Pathol* 2021;**34**:637–46. https://doi.org/10.1038/s41379-020-0614-0
36. Gascard P, Tlsty TD. Carcinoma-associated fibroblasts: orchestrating the composition of malignancy. *Genes Dev.* 2016;**30**:1002–19. https://doi.org/10.1101/gad.279737.116
37. Philip M, Schietinger A. CD8$^+$ T cell differentiation and dysfunction in cancer. *Nat Rev Immunol* 2022;**22**:209–23. https://doi.org/10.1038/s41577-021-00574-3
38. Chow A, Perica K, Klebanoff CA *et al.* Clinical implications of T cell exhaustion for cancer immunotherapy. *Nat Rev Clin Oncol* 2022;**19**:775–90. https://doi.org/10.1038/s41571-022-00689-z
39. Krausgruber T, Fortelny N, Fife-Gernedl V *et al.* Structural cells are key regulators of organ-specific immune responses. *Nature* 2020;**583**:296–302. https://doi.org/10.1038/s41586-020-2424-4
40. Zhang YF, Lv X, Chen LM *et al.* The role and function of CLU in cancer biology and therapy. *Clin Exp Med* 2022;**23**:1375–91. https://doi.org/10.1007/s10238-022-00885-2
41. Pirkkala L, Nykänen P, Sistonen L. Roles of the heat shock transcription factors in regulation of the heat shock response and beyond. *FASEB J* 2001;**15**:1118–31. https://doi.org/10.1096/fj00-0294rev
42. Mikami Y, Kyokawa T, Hata S *et al.* Gastrointestinal immunophenotype in adenocarcinomas of the uterine cervix and related glandular lesions: a possible link between lobular endocervical glandular hyperplasia/pyloric gland metaplasia and 'adenoma malignum'. *Mod Pathol* 2004;**17**:962–72. https://doi.org/10.1038/modpathol.3800148
43. Carleton C, Hoang L, Sah S *et al.* A detailed immunohistochemical analysis of a large series of cervical and vaginal gastric-type adenocarcinomas. *Am J Surg Pathol* 2016;**40**:636–44. https://doi.org/10.1097/PAS.0000000000000578
44. Sassine D, Straubhar AM, Aghajanian C *et al.* Gastric-type adenocarcinoma of the cervix: Genomic drivers and clinical out-

comes. *JCO* 2020;**38**:6030. https://doi.org/10.1200/JCO.2020.38.15_suppl.6030

45. Mikami Y. Gastric-type mucinous carcinoma of the cervix and its precursors—historical overview. *Histopathology* 2020;**76**:102–11. https://doi.org/10.1111/his.13993
46. Lu SS, Shen DH, Zhao Y *et al.* Primary endocervical gastric-type adenocarcinoma: a clinicopathologic and immunohistochemical analysis of 23 cases. *Diagn Pathol* 2019;**14**:1–72. https://doi.org/10.1186/s13000-019-0852-y
47. Yang J, Peng Y, Ding Y *et al.* The clinicopathological and molecular characteristics of endocervical gastric-type adenocarcinoma and the use of claudin18.2 as a potential therapeutic target. *Mod Pathol* 2024;**37**:100569. https://doi.org/10.1016/j.modpat.2024.100569
48. Nishio S. Current status and molecular biology of human papillomavirus-independent gastric-type adenocarcinoma of the cervix. *J of Obstet and Gynaecol* 2023;**49**:1106–13. https://doi.org/10.1111/jog.15578
49. Quail DF, Joyce JA. Microenvironmental regulation of tumor progression and metastasis. *Nat Med* 2013;**19**:1423–37. https://doi.org/10.1038/nm.3394
50. Xiong JX, Wang SX, Chen T *et al.* Verteporfin blocks Clusterin which is required for survival of gastric cancer stem cell by modulating HSP90 function. *Int. J. Biol. Sci.* 2019;**15**:312–24. https://doi.org/10.7150/ijbs.29135
51. Hoter A, Naim HY. Heat shock proteins and ovarian cancer: important roles and therapeutic opportunities. *Cancers* 2019;**11**:1389. https://doi.org/10.3390/cancers11091389
52. Birbo B, Madu EE, Madu CO *et al.* Role of HSP90 in cancer. *Int J Mol Sci* 2021;**22**:10317. https://doi.org/10.3390/ijms221910317
53. Morii T, Ohtsuka K, Ohnishi H *et al.*.Inhibition of heat-shock protein 27 expression eliminates drug resistance of osteosarcoma to zoledronic acid. *Anticancer Res* 2020; **30**:3565–71.
54. Trougakos IP, So A, Jansen B *et al.* Silencing expression of the clusterin/apolipoprotein J gene in human cancer cells using small interfering RNA induces spontaneous apoptosis, reduced growth ability, and cell sensitization to genotoxic and oxidative stress. *Cancer Res* 2004;**64**:1834–42. https://doi.org/10.1158/0008-5472.CAN-03-2664
55. Lamoureux F, Thomas C, Yin MJ *et al.* Clusterin inhibition using ogx-011 synergistically enhances hsp90 inhibitor activity by suppressing the heat shock response in castrate-resistant prostate cancer. *Cancer Res* 2011;**71**:5838–49. https://doi.org/10.1158/0008-5472.CAN-11-0994
56. Lamoureux F, Baud'huin M, Ory B *et al.* Clusterin inhibition using OGX-011 synergistically enhances zoledronic acid activity in osteosarcoma. *Oncotarget* 2014;**5**:7805–19. https://doi.org/10.18632/oncotarget.2308
57. Jiang VC, Hao DP, Jain P *et al.* TIGIT is the central player in T-cell suppression associated with CAR T-cell relapse in mantle cell lymphoma. *Mol Cancer* 2022;**21**:185. https://doi.org/10.1186/s12943-022-01655-0
58. Yang P, Yang ZY, Dong YM *et al.* Clusterin is a biomarker of breast cancer prognosis and correlated with immune microenvironment. *Translational Cancer Research* 2023;**12**: 31–45. https://doi.org/10.21037/tcr-22-1882
59. Cheng HX, Wang SK, Huang AD *et al.* HSF1 is involved in immunotherapeutic response through regulating APOJ/STAT3-mediated PD-L1 expression in hepatocellular carcinoma. *Cancer Biol Ther* 2023;**24**:1–9. https://doi.org/10.1080/15384047.2022.2156242
60. Tewari KS, Sill MW, Long HJ *et al.* Improved survival with bevacizumab in advanced cervical cancer. *N Engl J Med* 2014;**370**:734–43. https://doi.org/10.1056/NEJMoa1309748
61. Nishio S, Matsuo K, Nasu H *et al.* Analysis of postoperative adjuvant chemotherapy in 102 patients with gastric-type mucinous carcinoma of the uterine cervix: A multi-institutional study. *Ann Oncol* 2021;**32**:S759. https://doi.org/10.1016/j.annonc.2021.08.1234
62. García-Aranda M, Téllez T, Muñoz M *et al.* Clusterin inhibition mediates sensitivity to chemotherapy and radiotherapy in human cancer. *Anticancer Drugs* 2017;**28**:702–16. https://doi.org/10.1097/CAD.0000000000000507
63. Ma XK, Zou LY, Li X *et al.* MicroRNA-195 regulates docetaxel resistance by targeting clusterin in prostate cancer. *Biomed Pharmacother* 2018;**99**:445–50. https://doi.org/10.1016/j.biopha.2018.01.088
64. Zhang B, Liu ZM, Hao FG *et al.* siRNA-directed clusterin silencing promotes cisplatin antitumor activity in human non-small cell lung cancer xenografts in immunodeficient mice. *Eur Rev Med Pharmacol Sci* 2014;**18**:1595–601.
65. Ma Y, Yang QQ, Gu DM *et al.* Canadine inhibits epithelial mesenchymal transformation of HPV-negative cervical cancer. *Tissue Barriers* 2024;**12**: 2256641. https://doi.org/10.1080/21688370.2023.2256641
66. Zielinski R, Chi KN. Custirsen (OGX-011): a second-generation antisense inhibitor of clusterin in development for the treatment of prostate cancer. *Future Oncol* 2012;**8**:1239–51. https://doi.org/10.2217/fon.12.129
67. Chia S, Dent S, Ellard S *et al.* Phase II trial of OGX-011 in combination with docetaxel in metastatic breast cancer. *Clin Cancer Res* 2009;**15**:708–13. https://doi.org/10.1158/1078-0432.CCR-08-1159

Received: 28 October 2025. **Revised:** 25 January 2026. **Accepted:** 3 February 2026